Verification and convergence study of a spectral-element numerical methodology for fluid-structure interaction

YiQin Xu, Yulia T. Peet *

School for Engineering of Matter, Transport and Energy, Arizona State University, Tempe, AZ 85287, USA

ARTICLE INFO

ABSTRACT

A high-order in space spectral-element methodology for the solution of a strongly coupled fluid-structure interaction (FSI) problem is developed. A methodology is based on a partitioned solution of incompressible fluid equations on body-fitted grids, and nonlinearly-elastic solid deformation equations coupled via a fixed-point iteration approach with Aitken relaxation. A comprehensive verification strategy of the developed methodology is presented, including h-, p- and temporal refinement studies. An expected order of convergence is demonstrated first separately for the corresponding fluid and solid solvers, followed by a self-convergence study on a coupled FSI problem (self-convergence refers to a convergence to a reference solution obtained with the same solver at higher resolution). To this end, a new three-dimensional fluid-structure interaction benchmark is proposed for a verification of the FSI codes, which consists of a fluid flow in a channel with one rigid and one flexible wall. It is shown that, due to a consistent problem formulation, including initial and boundary conditions, a high-order spatial convergence on a fully coupled FSI problem can be demonstrated. Finally, a developed framework is applied successfully to a Direct Numerical Simulation of a turbulent flow in a channel interacting with a compliant wall, where the fluid-structure interface is fully resolved.

1. Introduction

A situation where a tight interaction occurs between a fluid flow and a surrounding structure, the so called fluid-structure interaction (FSI) problem, is prevalent in many engineering and biological applications. One famous example of a destabilizing effect of the fluid-structure interaction is the failure of the Tacoma Narrows bridge [1], while many other examples can be found in aerospace (flutter of airplane wings [2]), turbomachinery (turbine blade vibrations [3]) and nuclear (fretting in nuclear reactors [4]) engineering. FSI effects can also be beneficial; for example, compliant surfaces can delay laminar-to-turbulent transition [5,6], and, perhaps, reduce skin friction drag [7].

The problem of fluid-structure interaction is inevitably complex, featuring nonlinear interactions, tightly coupled multi-physical phenomena, and potential instabilities [8]. Accurate numerical solution of the FSI problem, even in relatively simple situations, is thus increasingly challenging. In many of the applications, the flow that interacts with a deformable surface is in a turbulent regime, which makes the computation of the FSI problem even more complicated, due to a wide range length and time scales that need to be resolved. High-order methods, such as spectral-element methods [9] and discontinuous Galerkin methods [10], have proven to be accurate and robust in application to scale-resolving simulations of turbulent

flows [11]. Computational methodologies that achieve high rates of convergence in the presence of fluid-structure interactions would thus be increasingly useful to the engineering and physical communities.

There are only a few examples in the literature that are concerned with a numerical discretization of the FSI problem with high-order methods. The authors of [12,13] employ spectral-element methods in the FSI problem discretization, Froehle & Persson [14] present an application of discontinuous Galerkin (DG) methods to a solution of the fluid-structure interaction problem involving compressible flows, Sheldon et al. [15] use hybridizable DG methods in incompressible FSI (although only first- and second-order elements were employed in the fully coupled FSI test cases), while Verkaik et al. [16] present an overlapping domain approach that couples low-order finite element methods in the vicinity of a deformable structure, with high-order spectral elements in a background mesh. One should also mention the work of [17] and references therein who use non-uniform rational B-spline isogeometric methods for fluid-structure interaction. While these developments have appeared, a strict verification of high-order convergence in the presence of complex multi-physics interactions remains a challenging task. Most of the researchers have resorted to a verification of the component solutions separately, such as only fluid or only solid. Thus, Ref. [18] presents h/p-convergence of an elastostatics solid solver with spectral elements, while [19] shows both h/p- and temporal convergence of the corresponding elastodynamics solver. Several groups demonstrate h/p- and/or temporal convergence of their fluid components of the FSI solvers on stationary ([20]) and deforming ([14,21,22]) domains, [15] presents a verification of h/p-convergence for both the fluid and the structural solvers separately using the method of manufactured solutions (MMS), while [16] does not show any convergence studies.

The current paper presents a recently developed high-order in space computational methodology for a solution of the fluid-structure interaction problem, together with a comprehensive verification strategy demonstrating the high-order spatial accuracy and up to a second-order temporal accuracy of the approach. The methodology is based on a spectral-element implementation [23] of both the Navier-Stokes, and the solid mechanics equations, where a hyperelastic St. Venant-Kirchhoff material model is employed for the solid [24,25]. The coupling between the fluid and solid components is performed in a partitioned manner, whereby a fixed point iteration [26] with Aitken relaxation [27] is employed to achieve a strong fluid-solid coupling. We admit that the fixed-point iteration with Aitken relaxation is not the state-of-the art method, and recent research has been devoted to a development of stable coupling methods with reduced amount of iterations [28–32]. However, the focus of this paper is on verification of the global h/p-spectral convergence of the methodology, while future work will be devoted to an acceleration of the FSI iterations.

A typical verification strategy of the FSI algorithms, apart from the component testing, is a simulation of a suite of accepted benchmark problems, one of which is a two-dimensional test case proposed by Turek & Hron [33], where a flow-induced vibration of a flexible beam attached to a rigid circular cylinder is studied numerically. Another variant of a similar test problem exists where a circular cylinder is replaced by a square cylinder [34]. In the absence of reliable experimental benchmarks for a fluid-structure interaction problem, the two aforementioned test cases have essentially taken a role of "validation experiments" in the FSI computational community, albeit the efforts to establish reliable experimental benchmarks for the FSI problems are underway [35]. While simulations on different levels of grid refinement are often performed with these two benchmarks [15,16,33], the verification of convergence rates is not demonstrated. Formaggia et al. [36], as well as Bathe & Ledezma [37], presented several three-dimensional computational test cases for the FSI problems, but, again, without demonstrating the formal rates of convergence. Fernández et al. [38] used self-convergence studies with a finite-element method in a two-dimensional pressure-driven pipe flow with a flexible wall, while Banks et al. [32] used both a method of manufactured solutions, as well as the traveling wave exact solutions of the 2D model FSI problems for the acoustic and linearly elastic solids to test their finite difference FSI code. Both studies were able to demonstrate a globally second-order spatial convergence on model FSI problems. A high-order convergence of the FSI methodologies on fully coupled FSI problems has not been demonstrated yet.

The current paper presents a new three-dimensional computational benchmark, on which the convergence properties of the FSI algorithms can be studied. The benchmark is inspired by a problem of the interaction of compliant surfaces with the fluid flow [39–41], and consists of a three-dimensional channel with one rigid and one flexible wall. We demonstrate the expected h/p-spatial convergence and the second order temporal convergence of the developed spectral-element FSI solver using this problem. Since the reference results are obtained with a high-order code on a well-resolved mesh, these data can be used by the computational community to test the convergence rate of their FSI codes, both low- and high-order accurate. While the current fixed-point iteration fluid-solid coupling algorithm is fairly standard, it is nonetheless widely used in many commercial and research FSI codes, as the more efficient alternatives are hard to implement [42]. With a fixed-point iteration algorithm, the computational efficiency can always be achieved by increasing the solver tolerances. In this paper, we demonstrate the effect of increasing the tolerances in both component and the coupling algorithms on the global computational errors. Additionally, we provide recommendations for acceptable tolerances with respect to their effect on the global errors. While convergence of the iterative algorithms in the FSI literature in terms of the iteration count has been studied extensively [13,26,30], the effect of these different strategies on errors has not been highlighted. The current study serves to fill this gap. Finally, we demonstrate the application of the developed high-order methodology to a Direct Numerical Simulation of a three-dimensional turbulent channel flow interacting with a hyperelastic solid wall, which shows the robustness of the methodology in the presence of the multiscale fluid-solid interactions.

The paper is organized as follows. Section 2 presents the numerical methodology for the solid and the fluid components, and their coupling. Section 3 demonstrates the h/p- and temporal convergence of the solid and fluid components separately. Section 4 verifies the performance of the coupled FSI solver on the traditional two-dimensional [33] and three-

dimensional [36,38] benchmark problems by comparing with the results of the other codes. Section 5 presents the new three-dimensional FSI benchmark, verifies a global h/p-convergence and a second-order temporal convergence of the developed FSI methodology using self-convergence tests, and presents the solver tolerance study. Section 6 applies the developed methodology to a turbulent fluid-structure interaction problem, while Section 7 draws conclusions.

2. Numerical method

The simulation domain $\Omega(t) \subset \mathbb{R}^3$ is decomposed into two separate nonoverlapping conforming subdomains $\Omega_s(t)$ and $\Omega_f(t)$, representing solid and fluid components, with their respective Dirichlet and Neumann boundaries $\partial\Omega_{s_D}(t)$, $\partial\Omega_{s_N}(t)$ and $\partial\Omega_{f_D}(t)$, $\partial\Omega_{f_N}(t)$. Additionally, common boundary $\Gamma_{fsi}(t) = \Omega_s(t) \cap \Omega_f(t)$ denotes the interface between the solid and the fluid domains with a full connectivity. The remainder of this section presents a mathematical formulation a numerical discretization of the solid and fluid equations, and their coupling.

2.1. Governing equations

2.1.1. Nonlinear structural mechanics

A nonlinear elasticity formulation allows for finite-size deformations, as opposed to a linear elasticity approach, considered, e.g., in [43]. Nonlinearity can be introduced from a geometry, material properties, kinematics and force [24,25]. Nonlinear solid equations in a strong form are written as

$$\rho_s \ddot{\mathbf{d}} = \nabla \cdot \sigma_s + \rho_s \mathbf{f} \text{ in } \Omega_s(t), \tag{1}$$

with the initial conditions

$$\begin{aligned}
\mathbf{d}(\mathbf{x}, t=0) &= \mathbf{d}_0(\mathbf{x}) \text{ in } \Omega_s(0), \\
\dot{\mathbf{d}}(\mathbf{x}, t=0) &= \mathbf{v}_0(\mathbf{x}) \text{ in } \Omega_s(0), \\
\ddot{\mathbf{d}}(\mathbf{x}, t=0) &= \mathbf{a}_0(\mathbf{x}) \text{ in } \Omega_s(0),
\end{aligned} \tag{2}$$

and boundary conditions

$$\mathbf{d}(\mathbf{x}, t) = \mathbf{d}_D(\mathbf{x}, t) \text{ on } \partial\Omega_{s_D}(t), \tag{3}$$

$$\sigma_s(\mathbf{x}, t) \cdot \mathbf{n} = \mathbf{T}_N(x, t) \text{ on } \partial\Omega_{s_N}(t) \cup \Gamma_{fsi}(t), \tag{4}$$

where $\dot{\mathbf{d}}, \ddot{\mathbf{d}}$ denote the first and the second partial temporal derivatives of the displacement $\mathbf{d} = \{d_x, d_y, d_z\}$, σ is the Cauchy stress tensor, and $\mathbf{T} = \{T_x, T_y, T_z\}$ is the surface traction. To solve the equations (1)–(4) in a spectral-element method, a weak form of Eq. (1) in a total Lagrangian formulation is stated as: find $\mathbf{d} \in \mathcal{H}_0^1(\Omega_s)$, such that $\forall \mathbf{w} \in \mathcal{H}_0^1(\Omega_s)$,

$$\int_{\Omega_s(0)} \mathbf{w} \cdot \rho_{s(0)} \ddot{\mathbf{d}} \, d\Omega + \int_{\Omega_s(0)} \nabla_0 \mathbf{w} : \mathbf{P} \, d\Omega - \int_{\Omega_s(0)} \mathbf{w} \cdot \rho_{s(0)} \mathbf{f} \, d\Omega - \int_{\Gamma_s(0)} \mathbf{w} \cdot \hat{\mathbf{T}} \, d\Gamma = 0. \tag{5}$$

Here, $\mathcal{H}_0^1(\Omega_s)$ denotes the Sobolev space of vector functions, vanishing to zero on a Dirichlet boundary, the solid domain boundary surface is defined as $\Gamma_s(0) = \partial\Omega_{s_N}(0) \cup \partial\Omega_{s_D}(0) \cup \Gamma_{fsi}(0)$, $\rho_{s(0)}$ is the initial solid density, which, in general, is time-dependent, ∇_0 refers to a gradient operator taken with respect to an initial configuration, $\hat{\mathbf{T}}$ is the equivalent traction on the reference surface from the Nanson's formula [17], $\mathbf{P} = \mathbf{FS}$ is the first Piola-Kirchhoff stress, which could be expressed by the deformation gradient $\mathbf{F}$ and the second Piola-Kirchhoff stress $\mathbf{S}$. The terms in Eq. (5) are transferred to the initial domain $\Omega_s(0)$ using a large deformation theory [24,44] through a valid mapping from an undeformed material point $\mathbf{X}$ to a deformed point $\mathbf{x}$. Such deformation could be described by a deformation gradient as

$$\mathbf{F}(\mathbf{d}) = \frac{\partial \mathbf{x}}{\partial \mathbf{X}} = \mathbf{I} + \frac{\partial \mathbf{d}}{\partial \mathbf{X}} = \mathbf{I} + \nabla_0 \mathbf{d}. \tag{6}$$

Furthermore, the Green-Lagrange strain tensor matched with the engineering strain is defined as $\mathbf{E} = \frac{1}{2}(\mathbf{F}^T \mathbf{F} - \mathbf{I})$, and the determinant of the deformation gradient is $J = |\mathbf{F}|$, which indicates the volume change during the deformation.

St. Venant-Kirchhoff material [24,25] is used in this paper, which is an extension of the linear elasticity model that considers large deformations,

$$\mathbf{S} = \mathbf{D} : \mathbf{E}, \tag{7}$$

where $\mathbf{D}$ is a fourth-order stiffness tensor. For isotropic materials considered in the current paper, the stiffness tensor has only two independent material parameters λ_s and μ_s, and is written as

$$\mathbf{D} = \lambda_s \mathbf{I} \otimes \mathbf{I} + 2\mu_s \mathbf{I}_4, \tag{8}$$

where λ_s is the first Lame's coefficient, μ_s is the second Lame's coefficient (or shear modulus), $\mathbf{I}$ is the second-order identity tensor, $\otimes$ is the symbol for the tensor product, and $\mathbf{I}_4$ is the symmetric fourth-order identity tensor [24]. Under the property of Eq. (8), Eq. (7) simplifies to

$$\mathbf{S} = \lambda_s \operatorname{tr}(\mathbf{E})\mathbf{I} + 2\mu_s\mathbf{E}. \tag{9}$$

2.1.2. Navier-Stokes ALE formulation

The fluid equations are solved in the Arbitrary Lagrangian Eulerian (ALE) formulation. A strong form of the incompressible Navier-Stokes equations in the ALE formulation can be written as

$$\rho_f \left(\frac{\partial \mathbf{u}}{\partial t} \Big|_{\hat{\mathbf{x}}} + (\mathbf{u} - \mathbf{w}) \cdot \nabla\mathbf{u} - \mathbf{f} \right) + \nabla p - \mu \triangle \mathbf{u} = 0 \text{ in } \Omega_f(t), \tag{10}$$

$$\nabla \cdot \mathbf{u} = 0 \text{ in } \Omega_f(t), \tag{11}$$

with the initial condition

$$\mathbf{u}(\mathbf{x}, t = 0) = \mathbf{u}_0(\mathbf{x}) \text{ in } \Omega_f(0), \tag{12}$$

and boundary conditions

$$\mathbf{u}(\mathbf{x}, t) = \mathbf{u}_D(\mathbf{x}, t) \text{ on } \partial\Omega_{f_D}(t) \cup \Gamma_{fsi}(t), \tag{13}$$

$$\nabla\mathbf{u}(\mathbf{x}, t) \cdot \mathbf{n} = 0 \text{ on } \partial\Omega_{f_N}(t), \tag{14}$$

where ρ_f, $\mathbf{u} = \{u_x, u_y, u_z\}$, $\mathbf{f} = \{f_x, f_y, f_z\}$, p, μ and $\mathbf{w} = \{w_x, w_y, w_z\}$ are the fluid density, velocity, external force, pressure, dynamic viscosity and the mesh velocity, respectively, while $\mathbf{n}$ is the outward-pointing unit vector normal to the surface. With the ALE formulation, the current configuration $\Omega_f(t)$ is defined through an ALE map, $\mathcal{A}_t$,

$$\mathcal{A}_t : \Omega_f(0) \in \mathbf{R}^d \to \Omega_f(t) \in \mathbf{R}^d, \ \mathbf{x}(\hat{\mathbf{x}}, t) = \mathcal{A}_t(\hat{\mathbf{x}}), \tag{15}$$

where d is the number of dimensions, which maps a reference configuration $\Omega_f(0)$ to a current configuration $\Omega_f(t)$, while associating the point $\hat{\mathbf{x}} \in \Omega_f(0)$ with the point $\mathbf{x}(\hat{\mathbf{x}}, t) \in \Omega_f(t)$ [21,45,46]. The ALE derivative in Eq. (10), $\frac{\partial}{\partial t}\big|_{\hat{\mathbf{x}}}$, denotes the derivative with respect to time in the reference fluid domain $\Omega_f(0)$. The mesh velocity $\hat{\mathbf{w}}(\hat{\mathbf{x}}, t)$ with respect to a reference domain is defined as

$$\hat{\mathbf{w}}(\hat{\mathbf{x}}, t) = \frac{\partial \mathbf{x}}{\partial t}\Big|_{\hat{\mathbf{x}}}. \tag{16}$$

In the current formulation, the mesh velocity field $\hat{\mathbf{w}}(\hat{\mathbf{x}}, t)$ is obtained at each time instance t via a solution of a steady linear elastic equation [9,43]

$$\operatorname{div}(\lambda_e \operatorname{tr}(\boldsymbol{\epsilon})\mathbf{I} + 2\mu_e \boldsymbol{\epsilon}) = 0, \tag{17}$$

where

$$\boldsymbol{\epsilon} = \frac{1}{2}\left[\nabla\hat{\mathbf{w}} + \nabla(\hat{\mathbf{w}})^T\right], \tag{18}$$

λ_e, μ_e are user-defined elastic parameters, satisfying boundary conditions $\hat{\mathbf{w}}(\hat{\mathbf{x}}, t) = \hat{\mathbf{w}}_{int}(\hat{\mathbf{x}}, t)$ on the moving mesh boundary, $\Gamma_{fsi}(0)$, and $\hat{\mathbf{w}}(\hat{\mathbf{x}}, t) = 0$ on the other domain boundaries, such as inflow $\partial\Omega_{f_D}(0)$ and outflow $\partial\Omega_{f_N}(0)$. The mesh velocity $\hat{\mathbf{w}}(\hat{\mathbf{x}}, t)$ can be transformed into the current domain $\Omega_f(t)$ with the help of an inverse ALE map as

$$\mathbf{w}(\mathbf{x}, t) = \hat{\mathbf{w}}(\mathcal{A}_t^{-1}(\mathbf{x}), t) \text{ in } \Omega_f(t). \tag{19}$$

Note that, due to a no-slip condition at the solid boundaries of the fluid domain, including the fluid-structure interface, the mesh velocity $\mathbf{w}(\mathbf{x}, t)$ at the FSI interface $\Gamma_{fsi}(t)$ also represents the boundary condition for the fluid velocity in Eq. (13),

$$\mathbf{u}_D(\mathbf{x}, t) = \mathbf{w}(\mathbf{x}, t), \ \mathbf{x} \in \Gamma_{fsi}(t). \tag{20}$$

In the present work, a conservative formulation of the weak form of Eq. (10) and Eq. (11) is considered, which is stated as: find $\mathbf{u} \in \mathcal{H}_0^1(\Omega_f)$ and $p \in \mathcal{L}_0^2(\Omega_f)$ such that $\forall \mathbf{v} \in \mathcal{H}_0^1(\Omega_f)$ and $\forall q \in \mathcal{L}_0^2(\Omega_f)$,

$$\frac{\partial}{\partial t} \int_{\Omega_f(t)} \mathbf{v} \cdot \rho_f \mathbf{u} \, d\Omega + \int_{\Omega_f(t)} \mathbf{v} \cdot \rho_f [\mathbf{u} \cdot \nabla \mathbf{u} - \nabla \cdot (\mathbf{u}\mathbf{w}) - \mathbf{f}] \, d\Omega$$

$$- \int_{\Omega_f(t)} \nabla \mathbf{v} \cdot p \, d\Omega + \int_{\Omega_f(t)} \mu \nabla \mathbf{v} : \nabla \mathbf{u} \, d\Omega - \int_{\Gamma_f(t)} \mathbf{v} \cdot (\mu \nabla \mathbf{u} - p)\mathbf{n} \, d\Gamma = 0, \tag{21}$$

$$\int_{\Omega_f(t)} q \cdot \nabla \mathbf{u} \, d\Omega = 0. \tag{22}$$

Here $\mathcal{H}_0^1(\Omega_f)$ denotes the Sobolev space of vector functions, vanishing to zero on a Dirichlet boundary, and $\mathcal{L}_0^2(\Omega_f)$ denotes the Hilbert space of vector functions that are square-integrable and have a zero mean value over the essential (pressure) boundary. $\Omega_f(t)$ and $\Gamma_f(t) = \partial\Omega_{f_D}(t) \cup \partial\Omega_{f_N}(t) \cup \Gamma_{fsi}(t)$ refer to a fluid current integration domain and its boundary surface, respectively. Further details, including the derivation of the conservative ALE formulation, can be found, for example, in [45,46].

2.1.3. Fluid-structure interaction

In a fluid-structure interaction problem, the solution of the solid and fluid equations is coupled through appropriate boundary conditions, which can be stated as

$$\mathbf{u}_D(\mathbf{x}, t) = \dot{\mathbf{d}}(\mathbf{x}, t) \text{ on } \Gamma_{fsi}(t), \tag{23}$$

$$\sigma_s(\mathbf{x}, t) \cdot (-\mathbf{n}_s) = \sigma_f(\mathbf{x}, t) \cdot \mathbf{n}_f \text{ on } \Gamma_{fsi}(t). \tag{24}$$

Here, σ_s is the Cauchy stress tensor of the solid, see Eq. (1), Eq. (4), and σ_f is the Cauchy stress tensor of the fluid defined as

$$\sigma_f(\mathbf{x}, t) = -p\mathbf{I} + \mu \left(\nabla \mathbf{u} + (\nabla \mathbf{u})^T \right), \tag{25}$$

and the outward unit surface normal vectors $\mathbf{n}_s$ and $\mathbf{n}_f$ for the solid and the fluid domains defined on the $\Gamma_{fsi}(t)$ boundary are pointing in opposite directions. The first boundary condition, Eq. (23), represents the kinematic constraint that the velocity on the interface $\Gamma_{fsi}(t)$ should be same in the fluid and the solid domains, and the second boundary condition, Eq. (24), reflects the continuity of the traction force across the interface.

Fluid-structure coupling in a partitioned manner is accomplished via a Dirichlet-Neumann approach, where the fluid uses velocity provided by the solid solution at the FSI interface as the Dirichlet boundary conditions, and the solid employs the traction supplied by the fluid as the Neumann boundary conditions, as reflected in Eq. (4), Eq. (13).

2.2. Temporal discretization

The current section describes the temporal discretization of the ALE fluid equations and the nonlinear solid mechanics equations. Both solid and fluid domains are discretized with the second-order methods. For the solid equations which contain the second order temporal derivative, a Newmark β-method with a constant average acceleration is employed [47], which is a second-order accurate implicit method commonly used for the time discretization of the structural dynamics equations [44]. For the fluid equations, a second-order accurate backward-differentiation scheme (BDF2) is employed [9,45]. The rest of this section provides the details of the two discretization schemes and the iteration procedures.

2.2.1. Solid temporal discretization

A. Newmark β method. For the solid temporal discretization, we employ the Newmark β scheme [47] with the parameters $(\beta, \gamma) = (0.25, 0.5)$, also known as a constant average acceleration method, wherein the velocity and acceleration at time step $n + 1$ can be expressed through the unknown displacements $\mathbf{d}^{n+1}$ as

$$\dot{\mathbf{d}}^{n+1} = \frac{2}{\delta t}(\mathbf{d}^{n+1} - \mathbf{d}^n) - \dot{\mathbf{d}}^n,$$

$$\ddot{\mathbf{d}}^{n+1} = \frac{4}{\delta t^2}(\mathbf{d}^{n+1} - \mathbf{d}^n) - \frac{4}{\delta t}\dot{\mathbf{d}}^n - \ddot{\mathbf{d}}^n, \tag{26}$$

where δt is the time step. For $(\beta, \gamma) = (0.25, 0.5)$, the Newmark scheme is second-order accurate and unconditionally stable under linear analysis [47]. As in [19], we have found this scheme to be stable with spectral-element discretization for the nonlinear structural dynamics problems simulated. When these expressions are substituted into the structural dynamics equation, Eq. (5), it becomes a nonlinear equation for displacement $\mathbf{d}^{n+1}$, which can be solved iteratively.

B. Newton-Raphson iterative procedure. To solve the nonlinear structural dynamics equation for displacements $\mathbf{d}^{n+1}$ with the implicit Newmark method, a Newton-Raphson iterative procedure [17,44,48] will be used. Instead of solving Eq. (5) directly, we solve for the increment of the displacement $\delta\mathbf{d}_{i+1}^{n+1}$ at each iteration $i+1$ at a time step $n+1$, i.e. we define $\delta\mathbf{d}_{i+1}^{n+1} = \mathbf{d}_{i+1}^{n+1} - \mathbf{d}_i^{n+1}$, and use linearization of Eq. (5) as

$$\frac{\partial\,\mathbf{N}}{\partial\,\mathbf{d}}\bigg|_{\mathbf{d}_i^{n+1}} \delta\mathbf{d}_{i+1}^{n+1} = -\mathbf{N}(\mathbf{d}_i^{n+1}), \tag{27}$$

where $\mathbf{N}(\mathbf{d}_i^{n+1})$ is the left-hand side of Eq. (5) evaluated at the previously known displacement $\mathbf{d}_i^{n+1}$, and the Jacobian matrix $(\partial\mathbf{N}/\partial\mathbf{d})|_{\mathbf{d}_i^{n+1}}$ is evaluated by solving the equation [24]

$$\frac{\partial\,\mathbf{N}}{\partial\,\mathbf{d}}\bigg|_{\mathbf{d}_i^{n+1}} \delta\mathbf{d}_{i+1}^{n+1} = \frac{\partial}{\partial\epsilon}\mathbf{N}(\mathbf{d}_i^{n+1} + \epsilon\delta\mathbf{d}_{i+1}^{n+1})\bigg|_{\epsilon=0}. \tag{28}$$

Setting the initial value $\mathbf{d}_0^{n+1}$ to be equal to a converged value of the displacement $\mathbf{d}^n$ from the previous time step, and after a linearization using Eq. (27) and Eq. (28), a nonlinear structural dynamic equation, Eq. (5), can then be solved as

$$\begin{aligned}
(\frac{4\mathbf{M}}{\delta t^2} + \mathbf{K})\,\delta\mathbf{d}_{i+1}^{n+1} = &\int\limits_{\Omega_s(0)} \mathbf{w}\cdot\rho_{s(0)}\mathbf{f}^{n+1}\,\mathrm{d}\Omega + \int\limits_{\Gamma_s(0)} \mathbf{w}\cdot\hat{\mathbf{T}}^{n+1}\,\mathrm{d}\Gamma \\
&- \int\limits_{\Omega_s(0)} \mathbf{S}_i^{n+1}:\bar{\mathbf{E}}_i^{n+1}\,\mathrm{d}\Omega - \mathbf{M}[\frac{4}{\delta t^2}(\mathbf{d}_i^{n+1} - \mathbf{d}^n) + \frac{4}{\delta t}\dot{\mathbf{d}}^n - \ddot{\mathbf{d}}^n],
\end{aligned} \tag{29}$$

with the mass matrix $\mathbf{M}$, stiffness matrix $\mathbf{K}$, and the other corresponding matrices defined as

$$\begin{aligned}
\mathbf{M}\delta\mathbf{d}_{i+1}^{n+1} &= \int\limits_{\Omega_s(0)} \mathbf{w}\cdot\rho_{s(0)}\delta\mathbf{d}_{i+1}^{n+1}\,\mathrm{d}\Omega, \\
\mathbf{K}\delta\mathbf{d}_{i+1}^{n+1} &= \int\limits_{\Omega_s(0)} (\delta\mathbf{S}_{i+1}^{n+1}:\bar{\mathbf{E}}_i^{n+1} + \mathbf{S}_i^{n+1}:\delta\bar{\mathbf{E}}_{i+1}^{n+1})\,\mathrm{d}\Omega, \\
\mathbf{S}_i^{n+1} &= \mathbf{D}:\mathbf{E}_i^{n+1}, \\
\bar{\mathbf{E}}_i^{n+1} &= \frac{1}{2}[\nabla_0\mathbf{w}^T\mathbf{F}(\mathbf{d}_i^{n+1}) + (\nabla_0\mathbf{w}^T\mathbf{F}(\mathbf{d}_i^{n+1}))^T], \\
\delta\mathbf{S}_{i+1}^{n+1} &= \mathbf{D}:\delta\mathbf{E} = \mathbf{D}:\frac{1}{2}[\nabla_0(\delta\mathbf{d}_i^{n+1})^T\mathbf{F}(\mathbf{d}_i^{n+1}) + (\nabla_0(\delta\mathbf{d}_i^{n+1})^T\mathbf{F}(\mathbf{d}_i^{n+1}))^T], \\
\delta\bar{\mathbf{E}}_{i+1}^{n+1} &= \frac{1}{2}[\nabla_0\mathbf{w}^T\nabla_0\delta\mathbf{d}_{i+1}^{n+1} + (\nabla_0\mathbf{w}^T\nabla_0\delta\mathbf{d}_{i+1}^{n+1})^T].
\end{aligned} \tag{30}$$

Once the increment of the displacement $\delta\mathbf{d}_{i+1}^{n+1}$ is obtained via solving Eq. (29) with the preconditioned conjugate gradient method (PCG), where the inverse of a spectral-element mass matrix is used as a preconditioner (mass matrix is diagonal in spectral elements, see Sec. 2.3), the solid displacement field can be updated as $\mathbf{d}_{i+1}^{n+1} = \mathbf{d}_i^{n+1} + \delta\mathbf{d}_{i+1}^{n+1}$. The iteration process is terminated when $\kappa_{s,\,i+1} = \|\delta\mathbf{d}_{i+1}^{n+1}\|_2/\|\mathbf{d}_i^{n+1}\|_2$ reaches a prescribed tolerance value κ_s. The value of the solid solver tolerance $\kappa_s = 10^{-12}$ is used in all the test cases in the current paper. Solid equations manifest good convergence properties, which permits such a tight tolerance to be set without affecting the overall solver cost. Note that the unknown surface traction $\hat{\mathbf{T}}^{n+1}$ at the FSI interface is provided by the solution of the fluid equations, and is updated implicitly during the partitioned fixed-point iteration coupling approach as discussed later.

2.2.2. Fluid temporal discretization
A. Backward-differentiation scheme. A backward-differentiation scheme of the second-order accuracy (BDF2) is used for the temporal discretization of the fluid equations. Applying BDF2 to Eq. (21) and Eq. (22) while denoting the current unknown time step with the superscript $n+1$ and the time step size as δt, transforms the fluid equations into the following semi-discrete form

$$\frac{3}{2\delta t} \int\limits_{\Omega_f(t^{n+1})} \mathbf{v} \cdot \rho_f \mathbf{u}^{n+1} \, d\Omega - \frac{2}{\delta t} \int\limits_{\Omega_f(t^n)} \mathbf{v} \cdot \rho_f \mathbf{u}^n \, d\Omega + \frac{1}{2\delta t} \int\limits_{\Omega_f(t^{n-1})} \mathbf{v} \cdot \rho_f \mathbf{u}^{n-1} \, d\Omega$$

$$= - \int\limits_{\Omega_f(t^{n+1})} \mu \nabla \mathbf{v} : \nabla \mathbf{u}^{n+1} \, d\Omega - \int\limits_{\Omega_f(t^{n+1})} \mathbf{v} \cdot \rho_f (\mathbf{u}^{n+1} \cdot \nabla \mathbf{u}^{n+1}) \, d\Omega + \int\limits_{\Omega_f(t^{n+1})} \mathbf{v} \cdot \rho_f \mathbf{f}^{n+1} \, d\Omega + \tag{31}$$

$$\int\limits_{\Omega_f(t^{n+1})} \nabla \mathbf{v} \cdot p^{n+1} \, d\Omega + \int\limits_{\Gamma_f(t^{n+1})} \mathbf{v} \cdot (\mu \nabla \mathbf{u}^{n+1} - p^{n+1}) \mathbf{n} \, d\Gamma + \int\limits_{\Omega_f(t^{n+1})} \mathbf{v} \cdot \rho_f [\nabla \cdot (\mathbf{u}^{n+1} \mathbf{w}^{n+1})] \, d\Omega,$$

$$\int\limits_{\Omega_f(t^{n+1})} q \cdot \nabla \mathbf{u}^{n+1} \, d\Omega = 0. \tag{32}$$

B. ALE geometry update. Note that in this, implicit, formulation, the Eq. (31) and Eq. (32) are solved in the current, updated configuration $\Omega_f(t^{n+1})$, associated with the current ALE map $\mathcal{A}_t^{n+1}(\hat{\mathbf{x}})$. Since the ALE map is closely linked to the mesh velocity via Eq. (16), a temporal discretization of the evolution equation, Eq. (16), would define the temporal discretization of the ALE map, which can, in principle, be decoupled from the temporal discretization of the governing fluid equations, Eq. (31) and Eq. (32). One obvious choice for a temporal discretization of Eq. (16) would be to use the BDF scheme of the same order as the discretization of the governing fluid equations, i.e. BDF2, as is done, for example, in stand-alone ALE developments [21,49]. However, in a fluid-structure interaction problem, the fluid geometry update should match the solid geometry update, otherwise there would be a discontinuity in the interface position which is undesirable. With the current constant average acceleration Newmark method for the solid discretization, it is seen from Eq. (26) that the solid geometry update

$$\mathbf{d}^{n+1} = \mathbf{d}^n + \frac{\delta t}{2}(\dot{\mathbf{d}}^{n+1} + \dot{\mathbf{d}}^n) \tag{33}$$

is essentially equivalent to a semi-implicit trapezoidal (or Crank-Nicholson) scheme. To match this update, we have explored two possibilities for the ALE map discretization:

1. First-order implicit Euler (IE) update: IE-ALE scheme,

$$\mathcal{A}_t^{n+1}(\hat{\mathbf{x}}) = \mathcal{A}_t^n(\hat{\mathbf{x}}) + \hat{\mathbf{w}}^{n+1}(\hat{\mathbf{x}}) \, \delta t. \tag{34}$$

   To match the solid and fluid displacement at the FSI boundary, the FSI interface velocity for the time interval $[t^n, t^{n+1}]$ is defined as

$$\hat{\mathbf{w}}_{int}^{n+1}(\hat{\mathbf{x}}) = \frac{1}{2}\left[\dot{\mathbf{d}}^{n+1}(\hat{\mathbf{x}}) + \dot{\mathbf{d}}^n(\hat{\mathbf{x}})\right] \in \Gamma_{fsi}(0), \tag{35}$$

   which is equivalent to approximating the integral $\hat{\mathbf{w}}_{int}^{n+1}(\hat{\mathbf{x}}) \, \delta t = \int_{t^n}^{t^{n+1}} \dot{\mathbf{d}}(\hat{\mathbf{x}}, t) \, dt$, $\hat{\mathbf{x}} \in \Gamma_{fsi}(0)$, with the trapezoidal rule.

2. Second-order semi-implicit (Crank-Nicholson) update: CN-ALE scheme,

$$\mathcal{A}_t^{n+1}(\hat{\mathbf{x}}) = \mathcal{A}_t^n(\hat{\mathbf{x}}) + \frac{\delta t}{2}\left[\hat{\mathbf{w}}^{n+1}(\hat{\mathbf{x}}) + \hat{\mathbf{w}}^n(\hat{\mathbf{x}})\right], \tag{36}$$

   where the mesh velocity at the interface $\hat{\mathbf{w}}_{int}^{n+1}(\hat{\mathbf{x}})$ is set equal to the corresponding structure velocity at a time step t^{n+1} from the solid solver:

$$\hat{\mathbf{w}}_{int}^{n+1}(\hat{\mathbf{x}}) = \dot{\mathbf{d}}^{n+1}(\hat{\mathbf{x}}), \ \hat{\mathbf{x}} \in \Gamma_{fsi}(0). \tag{37}$$

In both methods, after the FSI interface velocity conditions are set up by Eq. (35) or Eq. (37), the ALE mesh velocity $\hat{\mathbf{w}}^{n+1}(\hat{\mathbf{x}})$ in the entire domain is obtained via a solution of an elastic equation, Eq. (17), with the boundary conditions $\hat{\mathbf{w}}^{n+1}(\hat{\mathbf{x}}) = \hat{\mathbf{w}}_{int}^{n+1}(\hat{\mathbf{x}})$ on $\Gamma_{fsi}(0)$. Upon updating the ALE configuration via Eq. (34) or Eq. (36), the mesh velocity in the current configuration $\Omega_f(t^{n+1})$ used in Eq. (31) is obtained as

$$\mathbf{w}^{n+1}(\mathbf{x}) = \hat{\mathbf{w}}^{n+1} \circ (\mathcal{A}_t^{-1}(\mathbf{x}))^{n+1}. \tag{38}$$

C. Geometric conservation law. Note that the BDF2 scheme applied to a conservative formulation of the ALE equations, Eq. (31), does not satisfy the geometric conservation law (GCL) [46], which means that it can not reproduce a constant solution exactly. The role of GCL with respect to the accuracy and stability of numerical schemes on moving grids was investigated extensively in, e.g. [46,50–52]. It was shown in [46,52] that, in general, a satisfaction of the GCL is neither a

necessary nor sufficient condition for either accuracy or stability. However, in some situations, depending on a particular numerical scheme, GCL might be required to ensure certain numerical properties. For example, as shown in [46], a BDF2 scheme that does not satisfy the GCL law can achieve only first order time-accuracy if the ALE mesh geometry is updated linearly in time (as with Eq. (34)). It is, however, fairly straightforward to modify the BDF2 scheme given by Eqs. (31)–(32), so that the Geometric Conservation Law is satisfied [46,53], as

$$
\frac{3}{2\delta t} \int_{\Omega_f(t^{n+1})} \mathbf{v} \cdot \rho_f \mathbf{u}^{n+1}\, d\Omega - \frac{2}{\delta t} \int_{\Omega_f(t^n)} \mathbf{v} \cdot \rho_f \mathbf{u}^n\, d\Omega + \frac{1}{2\delta t} \int_{\Omega_f(t^{n-1})} \mathbf{v} \cdot \rho_f \mathbf{u}^{n-1}\, d\Omega
$$

$$
= - \int_{\Omega_f(t^{n+1})} \mu \nabla\mathbf{v} : \nabla\mathbf{u}^{n+1}\, d\Omega - \int_{\Omega_f(t^{n+1})} \mathbf{v} \cdot \rho_f (\mathbf{u}^{n+1} \cdot \nabla\mathbf{u}^{n+1})\, d\Omega + \int_{\Omega_f(t^{n+1})} \mathbf{v} \cdot \rho_f \mathbf{f}^{n+1}\, d\Omega +
$$

$$
\int_{\Omega_f(t^{n+1})} \nabla\mathbf{v} \cdot p^{n+1}\, d\Omega + \int_{\Gamma_f(t^{n+1})} \mathbf{v} \cdot (\mu\nabla\mathbf{u}^{n+1} - p^{n+1})\mathbf{n}\, d\Gamma + \frac{3}{2} \int_{\Omega_f(t^{n+1})} \mathbf{v} \cdot \rho_f [\nabla \cdot (\mathbf{u}^{n+1}\mathbf{w}^{n+1})]\, d\Omega -
$$

$$
\frac{1}{2} \int_{\Omega_f(t^n)} \mathbf{v} \cdot \rho_f [\nabla \cdot (\mathbf{u}^{n+1}\mathbf{w}^n)]\, d\Omega, \tag{39}
$$

$$
\int_{\Omega_f(t^{n+1})} q \cdot \nabla\mathbf{u}^{n+1}\, d\Omega = 0. \tag{40}
$$

It was shown in [46] that, for a model linear advection-diffusion equation discretized with finite-element methods, the GCL-satisfying BDF2 scheme in the form of Eq. (39) was able to attain a second-order temporal accuracy even with the linear in time ALE mesh update. Note that, with the ALE mesh interpolation scheme of order higher than one, satisfaction of the GCL is, in general, not necessary for achieving a global second-order temporal accuracy on moving meshes, as was the case, for example, in stand-alone ALE formulations (no FSI) [21,49], where the ALE geometry was updated with the BDF scheme of the same order as used for the discretization of the Navier-Stokes equations. While the behavior of the BDF2 schemes with the Crank-Nicholson (CN) type geometry update (see Eq. (36)) was not previously analyzed, the current numerical experiments show that, as expected, the GCL law is not necessary with the CN mesh update for achieving a global second-order time accuracy on moving grids on an example of a convecting eddy viscous flow solution, see Sec. 3.2. Consequently, the GCL BDF2 scheme, Eq. (39), is used with the first-order IE-ALE geometry update, and the no-GCL BDF2 scheme, Eq. (31), is used with the second-order CN-ALE geometry update.

D. Sub-iteration method. This section deals with the treatment of the non-linear convective term $\int_{\Omega_f(t^{n+1})} \mathbf{v} \cdot \rho_f (\mathbf{u}^{n+1} \cdot \nabla\mathbf{u}^{n+1})\, d\Omega$ (also, mesh velocity term $\int_{\Omega_f(t^{n+1})} \mathbf{v} \cdot \rho_f [\nabla \cdot (\mathbf{u}^{n+1}\mathbf{w}^{n+1})]\, d\Omega$ with moving domains) in Eq. (31), Eq. (39). One approach would be to treat this term (terms) explicitly via an extrapolation from the previous time steps, as is done, e.g., in [45,49,54]. This method produces stable and accurate results on stationary domains, and on moving domains where the movement of the domain boundary at the next time instance can be well predicted by extrapolation, as is the case, for example, with prescribed domain motions parameterized by a known function of time [45,49]. Our previous work [48] has shown, however, that with domain motions that can not be well predicted by extrapolation, such as, for example, with sudden, or impulsive, motions, the explicit approach fails to reproduce a stabilized pressure field in a short enough time. While the pressure recovery would eventually follow after a certain time lag, in a fully coupled FSI loop, a short-term disturbance of the pressure field would get amplified via an FSI iteration and lead to numerical instabilities. To avoid this situation, we follow, after [20], an implicit approach for the treatment of the non-linear convective term in the BDF2 formulation, in the form of sub-iterations.

In [20,48], sub-iterations are described in a strong form. Here, we develop a more appropriate mathematical formulation by introducing a sub-iteration approach in a weak form, since this is precisely the form that is being solved numerically in the weighted-residual based methods, such as a spectral-element method [9]. Following a similar approach as described in Sec. 2.2.1 in regards to an iterative solution of the nonlinear solid dynamics equations, both no-GCL and CGL ALE formulations given by Eqs. (31)–(32) and Eqs. (39)–(40), respectively, can be written in a form,

$$
\mathbf{N_M}(\mathbf{u}^{n+1}, p^{n+1}) = 0,
$$
$$
\mathbf{N_C}(\mathbf{u}^{n+1}) = 0, \tag{41}
$$

where $\mathbf{N_M}$ is a non-linear variational functional corresponding to the momentum equations, and $\mathbf{N_C}$ is the non-linear functional for the continuity equation, defined as the difference between the left-hand side and the right-hand side of Eq. (31), Eq. (39) for $\mathbf{N_M}$, and as the left-hand side of Eq. (32), Eq. (40) for $\mathbf{N_C}$. Note that the continuity equation does not contain pressure, so that the functional $\mathbf{N_C}$ in Eq. (41) is independent of the pressure term.

As in Sec. 2.2.1, introducing iterative corrections to the independent problem variables at each time step $n + 1$ and each iteration $i + 1$

$$
\begin{aligned}
\mathbf{u}_{i+1}^{n+1} &= \mathbf{u}_i^{n+1} + \delta \mathbf{u}_{i+1}^{n+1}, \\
p_{i+1}^{n+1} &= p_i^{n+1} + \delta p_{i+1}^{n+1},
\end{aligned}
\tag{42}
$$

and linearizing the system given by Eq. (41) around the previous known values $(\mathbf{u}_i^{n+1}, p_i^{n+1})$, a solution of the following linearized equations in a Newton-Raphson form is being sought,

$$
\begin{aligned}
\left. \frac{\partial \mathbf{N_M}}{\partial \mathbf{u}} \right|_{\mathbf{u}_i^{n+1}} \delta \mathbf{u}_{i+1}^{n+1} + \left. \frac{\partial \mathbf{N_M}}{\partial p} \right|_{p_i^{n+1}} \delta p_{i+1}^{n+1} &= -\mathbf{N_M}(\mathbf{u}_i^{n+1}, p_i^{n+1}), \\
\left. \frac{\partial \mathbf{N_C}}{\partial \mathbf{u}} \right|_{\mathbf{u}_i^{n+1}} \delta \mathbf{u}_{i+1}^{n+1} &= -\mathbf{N_C}(\mathbf{u}_i^{n+1}).
\end{aligned}
\tag{43}
$$

For evaluation of the Jacobian matrices, we omit nonlinear terms from the calculation of the Jacobians but keep them in the right-hand side of the iterative equation, Eq. (43), since Jacobians are not required to be exact with the implicit iterations procedure [20,48]. The linearized system, however, contains the implicit pressure-velocity relationship inherent to the incompressible Navier-Stokes equations system [9]:

$$
\begin{bmatrix} \mathcal{F} & \mathcal{G} \\ \mathcal{D} & 0 \end{bmatrix} \begin{bmatrix} \delta \mathbf{u}_{i+1}^{n+1} \\ \delta p_{i+1}^{n+1} \end{bmatrix} = \begin{bmatrix} -\mathbf{N_M}_i^{n+1} \\ -\mathbf{N_C}_i^{n+1} \end{bmatrix},
\tag{44}
$$

where

$$
\begin{aligned}
\mathcal{F} \delta \mathbf{u}_{i+1}^{n+1} &= \frac{3}{2 \delta t} \int\limits_{\Omega_f(t^{n+1})} \mathbf{v} \cdot \rho_f \, \delta \mathbf{u}_{i+1}^{n+1} \, d\Omega + \int\limits_{\Omega_f(t^{n+1})} \mu \nabla \mathbf{v} : \nabla \delta \mathbf{u}_{i+1}^{n+1} \, d\Omega, \\
\mathcal{G} \delta p_{i+1}^{n+1} &= - \int\limits_{\Omega_f(t^{n+1})} \nabla \mathbf{v} \cdot \delta p_{i+1}^{n+1} \, d\Omega, \\
\mathcal{D} \delta \mathbf{u}_{i+1}^{n+1} &= - \int\limits_{\Omega_f(t^{n+1})} q \cdot \nabla \delta \mathbf{u}_{i+1}^{n+1} \, d\Omega, \\
-\mathbf{N_M}_i^{n+1} &= \frac{2}{\delta t} \int\limits_{\Omega_f(t^n)} \mathbf{v} \cdot \rho_f \mathbf{u}^n \, d\Omega - \frac{1}{2 \delta t} \int\limits_{\Omega_f(t^{n-1})} \mathbf{v} \cdot \rho_f \mathbf{u}^{n-1} \, d\Omega - \int\limits_{\Omega_f(t^{n+1})} \mathbf{v} \cdot \rho_f (\mathbf{u}_i^{n+1} \cdot \nabla \mathbf{u}_i^{n+1}) \, d\Omega \\
&\quad + \int\limits_{\Omega_f(t^{n+1})} \mathbf{v} \cdot \rho_f \mathbf{f}^{n+1} \, d\Omega + \int\limits_{\Omega_f(t^{n+1})} \nabla \mathbf{v} \cdot p_i^{n+1} \, d\Omega + \int\limits_{\Gamma_f(t^{n+1})} \mathbf{v} \cdot (\mu \nabla \mathbf{u}^{n+1} - p^{n+1}) \mathbf{n} \, d\Gamma + \mathbf{g_w}(\mathbf{u}_i^{n+1}, t_i^{n+1}), \\
-\mathbf{N_C}_i^{n+1} &= 0,
\end{aligned}
\tag{45}
$$

and the mesh velocity term $\mathbf{g_w}(\mathbf{u}_i^{n+1}, t_i^{n+1})$ is equal to

$$
\mathbf{g_w}(\mathbf{u}_i^{n+1}, t_i^{n+1}) = \begin{cases} \frac{3}{2} \int_{\Omega_f(t^{n+1})} \mathbf{v} \cdot \rho_f [\nabla \cdot (\mathbf{u}_i^{n+1} \mathbf{w}^{n+1})] \, d\Omega - \frac{1}{2} \int_{\Omega_f(t^n)} \mathbf{v} \cdot \rho_f [\nabla \cdot (\mathbf{u}_i^{n+1} \mathbf{w}^n)] \, d\Omega, & \text{IE update with GCL} \\ \int_{\Omega_f(t^{n+1})} \mathbf{v} \cdot \rho_f [\nabla \cdot (\mathbf{u}_i^{n+1} \mathbf{w}^{n+1})] \, d\Omega, & \text{IE or CN update with no GCL.} \end{cases}
\tag{46}
$$

To solve the system of Eq. (44), following [9,55], we use inexact block LU factorization procedure as

$$
\begin{bmatrix} \mathcal{F} & \mathcal{G} \\ \mathcal{D} & 0 \end{bmatrix} \approx \begin{bmatrix} \mathcal{F} & 0 \\ \mathcal{D} & -\mathcal{D} \mathcal{Q}_1 \mathcal{G} \end{bmatrix} \begin{bmatrix} \mathbf{I} & \mathcal{Q}_2 \mathcal{G} \\ 0 & \mathbf{I} \end{bmatrix},
\tag{47}
$$

where $\mathcal{Q}_1$, $\mathcal{Q}_2$ serve to approximate an inverse of the matrix $\mathcal{F}^{-1}$, and in the current method are chosen as

$$
\mathcal{Q}_1 = \mathcal{Q}_2 = \frac{\delta t}{\beta_0} \mathcal{M}^{-1},
\tag{48}
$$

while other choices are possible [9,55]. Here, $\beta_0 = 3/2$ is the leading coefficient in the BDF scheme, and $\mathcal{M}$ is the mass matrix defined as

$$\mathcal{M}\,\delta\mathbf{u}_{i+1}^{n+1} = \int\limits_{\Omega_f(t^{n+1})} \mathbf{v} \cdot \rho_f\,\delta\mathbf{u}_{i+1}^{n+1}\,\mathrm{d}\Omega. \tag{49}$$

Note that an approximation of the matrix $\mathcal{F}^{-1}$ by inexact matrices $\mathcal{Q}_1$, $\mathcal{Q}_2$ generally (with explicit methods) results in splitting errors that can affect the overall accuracy of the temporal scheme. The splitting error with the current choice of $\mathcal{Q}_1$, $\mathcal{Q}_2$ would be of the order of $(\delta t)^2$ with the pressure-correction algorithm [9,56] and would not affect the accuracy of BDF2 in any case. However, in the current implicit method, the inexact factorization affects only the convergence of the iterations, and not a temporal accuracy of the scheme, which is not affected by the structure of the iteration matrix, so the choice of an inexact factorization in implicit methods is more forgiving.

With this inexact LU-factorization, a solution of the original system, Eq. (44), is equivalent to a solution of three split equations, with an intermediate velocity field $\delta\tilde{\mathbf{u}}_{i+1}^{n+1}$ introduced as an auxiliary variable [9,55]

$$\begin{aligned}
\mathcal{F}\,\delta\tilde{\mathbf{u}}_i^{n+1} &= -\mathbf{N_{M}}_i^{n+1}, \\
\mathcal{D}\,\mathcal{M}^{-1}\mathcal{G}\,\delta p_{i+1}^{n+1} &= \mathcal{D}\,\delta\tilde{\mathbf{u}}_{i+1}^{n+1}, \\
\mathcal{M}\,\delta\mathbf{u}_{i+1}^{n+1} &= \mathcal{M}\,\delta\tilde{\mathbf{u}}_{i+1}^{n+1} - \mathcal{G}\,\delta p_{i+1}^{n+1}.
\end{aligned} \tag{50}$$

The first equation in the system of Eq. (50) is in the form of a Helmholtz equation, and is solved by the PCG method with the inverse mass matrix as the preconditioner, and the second Poisson-like equation is solved by the Generalized Minimal Residual Method (GMRES) with a multi-grid preconditioning [9]. Note that in the current implementation of the spectral-element method, a discrete Helmholtz operator is symmetric positive definite [9,54], which makes it possible to use PCG solver for the Helmholtz equation. The velocity and the pressure fields are updated iteratively until $\kappa_{f,i+1} = \|\delta\mathbf{u}_{i+1}^{n+1}\|_2/\|\mathbf{u}_i^{n+1}\|_2 \le \kappa_f$ and $\kappa_{p,i+1} = \|\delta p_{i+1}^{n+1}\|_2/\|p_i^{n+1}\|_2 \le \kappa_p$. The baseline values of velocity and pressure tolerances are set to $\kappa_f = 10^{-6}, \kappa_p = 10^{-5}$ in all the test cases in the current paper, apart from the tolerance sensitivity study in Sec. 5, for which they are varying. When the velocity tolerance κ_f varies, the pressure tolerance is always set up as $\kappa_p = 10\kappa_f$. To accelerate convergence of the iterations, Aitken relaxation [27] is used as described below in Eq. (61), but acting on the velocity and pressure fields, $\mathbf{u}_i^{n+1}, p_i^{n+1}$.

2.3. Solid and fluid spatial discretization

To solve the solid domain equations of Eq. (5), with the Newmark method, Eq. (26), initial condition of Eq. (2), and boundary conditions of Eq. (3), Eq. (4), and the fluid domain equations in a no-GCL form of Eq. (31), Eq. (32), or a GCL form of Eq. (39), Eq. (40), initial condition, Eq. (12), and boundary conditions, Eq. (13), Eq. (14), a spectral element method (SEM) implemented in a solver Nek5000 [9] is employed, that ensures a high-order spectral convergence in space with p-refinement.

In a spectral-element formulation, the computational domain Ω_s or Ω_f is decomposed into a set of nonoverlapping adjacent elements Ω^e mapped from a reference element $\hat{\Omega}$. Variables from different search spaces $\mathcal{H}^1(\hat{\Omega})$ or $\mathcal{L}^2(\hat{\Omega})$ are projected onto subspaces $\mathbb{P}_N$, $\mathbb{P}_M$, where $M = N - 2$ in the current formulation. Thus, in a solid domain, the displacement field at a time step t^{n+1}, $\mathbf{d}_e^{n+1}(\boldsymbol{\xi}) \in \mathcal{H}^1(\hat{\Omega}_s)$ is discretized as

$$\mathbf{d}_e^{n+1}(\boldsymbol{\xi}) = \sum_{i=0}^{N}\sum_{j=0}^{N}\sum_{k=0}^{N} \mathbf{d}_{e,ijk}^{n+1}\pi_{N,i}(\xi_1)\pi_{N,j}(\xi_2)\pi_{N,k}(\xi_3), \quad \boldsymbol{\xi} \in \hat{\Omega}_s, \tag{51}$$

and in a fluid domain, the velocity field at a time step t^{n+1}, $\mathbf{u}_e^{n+1}(\boldsymbol{\xi}) \in \mathcal{H}^1(\hat{\Omega}_f)$, and the pressure $p_e^{n+1}(\tilde{\boldsymbol{\xi}}) \in \mathcal{L}^2(\hat{\Omega}_f)$ are represented as

$$\mathbf{u}_e^{n+1}(\boldsymbol{\xi}) = \sum_{i=0}^{N}\sum_{j=0}^{N}\sum_{k=0}^{N} \mathbf{u}_{e,ijk}^{n+1}\pi_{N,i}(\xi_1)\pi_{N,j}(\xi_2)\pi_{N,k}(\xi_3), \quad \boldsymbol{\xi} \in \hat{\Omega}_f, \tag{52}$$

$$p_e^{n+1}(\tilde{\boldsymbol{\xi}}) = \sum_{i=1}^{N-1}\sum_{j=1}^{N-1}\sum_{k=1}^{N-1} p_{e,ijk}^{n+1}\tilde{\pi}_{N-2,i}(\tilde{\xi}_1)\tilde{\pi}_{N-2,j}(\tilde{\xi}_2)\tilde{\pi}_{N-2,k}(\tilde{\xi}_3), \quad \tilde{\boldsymbol{\xi}} \in \hat{\Omega}_f. \tag{53}$$

Here, $\mathbf{d}_{e,ijk}^{n+1}$, $\mathbf{u}_{e,ijk}^{n+1}$, $p_{e,ijk}^{n+1}$, are the nodal values of displacements (for solid), velocity and pressure (for fluid), in the corresponding elements at a time step t^{n+1}, the basis functions $\pi_{N,\alpha}(\xi_\beta)$, $\tilde{\pi}_{N-2,\alpha}(\tilde{\xi}_\beta)$, $\alpha = \{i,j,k\}$, $\beta = \{1,2,3\}$, are the Lagrange interpolating polynomials of degree N, $N - 2$, respectively. For a high-order integration, the quadrature nodes are

defined as the Gauss-Lobatto-Legendre (GLL) nodes, $\xi_{\beta m, m=0, \ldots N}$, for $\mathbb{P}_N$ integration, and the Gauss-Legendre (GL) nodes, $\tilde{\xi}_{\beta m, m=1, \ldots N-1}$, for $\mathbb{P}_{N-2}$ integration. The Lagrange interpolating polynomials $\pi_{N,\alpha}(\xi_\beta)$, $\tilde{\pi}_{N-2,\alpha}(\tilde{\xi}_\beta)$, satisfy the properties

$$
\begin{aligned}
\pi_{N,\alpha}(\xi_{\beta m}) &= \delta_{\alpha m} \\
\tilde{\pi}_{N-2,\alpha}(\tilde{\xi}_{\beta m}) &= \delta_{\alpha m},
\end{aligned}
\tag{54}
$$

where $\delta_{\alpha m}$ is the Kronecker delta function.

With this discretization, the inner products in the governing equations for the solid and the fluid, Eq. (5), Eq. (31), Eq. (32), Eq. (39), Eq. (40), are evaluated using Gauss integration on the corresponding GLL or GL nodes on an element-by-element basis, and then assembled across the union of elements encompassing the solid and the fluid domains, respectively. Upon discretization and assembly, the inner products take a form of discrete matrix-vector products, where the matrices correspond to a discretized form of the mass, stiffness, and other spectral-element matrices as defined in Eq. (30), Eq. (44), while the vectors correspond to the unknown arrays $\mathbf{d}_{e,ijk}^{n+1}$, $\mathbf{u}_{e,ijk}^{n+1}$, $p_{e,ijk}^{n+1}$ across the solid and fluid elements. For deformed geometries, spectral-element matrices contain the Jacobian terms of the mapping functions between the physical element Ω^e and the reference element $\hat{\Omega}$. For a global assembly of the inner products across the elements, a connectivity operator $\mathcal{C}$ is used, which defines a gather, $\mathbf{d}^{n+1} = \mathcal{C}^T \mathbf{d}_L^{n+1}$, and scatter, $\mathbf{d}_L^{n+1} = \mathcal{C} \mathbf{d}^{n+1}$ operations, where $\mathbf{d}_L^{n+1}$ represent the local, unassembled, arrays, and $\mathbf{d}^{n+1}$ represent the global, assembled arrays, similarly for velocity and pressure. The gather-scatter operators then appear multiplicatively at the left and the right of the corresponding spectral-element matrix operators in the discretization of the inner products, see, Refs. [9,45,54,57] for more details. With the discretizations (52)–(51) and the property (54), the mass matrix is diagonal in spectral-element methods, and consists of the corresponding Gauss integration quadrature weights on the diagonal [9,57].

2.3.1. Fluid-structure interaction with partitioned coupling

A fluid-structure coupling is accomplished via a partitioned approach, which advances the fluid and solid equations iteratively with a fixed-point iteration algorithm using Aitken relaxation [26,27] to accelerate convergence of the iterations. The solid and fluid spectral-element meshes are matched at the FSI boundary, $\Gamma_{fsi}(0)$, at time $t = 0$, and, due to an ALE geometry update that guarantees the continuity of the displacements between the solid and fluid domains in a discrete sense, as described in Sec. 2.2.2, the congruence of the solid and fluid meshes is preserved at $\Gamma_{fsi}(t)$ at $t \geq 0$. Therefore, a simple exchange of the nodal values between the meshes is performed to communicate the corresponding solid and fluid variables to satisfy the coupling boundary conditions, and no spatial interpolation is required. The algorithm for the fluid-structure coupling that implicitly satisfies the fluid-structure interface boundary conditions, Eq. (23) and Eq. (24), thus reads as follows: at each new time step t^{n+1}

1. **Fluid**: Solve for $\mathbf{u}_{k=1}^{n+1}$ and $p_{k=1}^{n+1}$ via Eqs. (39), (40) (IE-ALE update), or (31), (32) (CN-ALE update), with the mesh velocity $\mathbf{w}_{k=1}^{n+1}$ calculated from Eq. (17), Eq. (38) using boundary conditions

$$
\hat{\mathbf{w}}_{int,k=1}^{n+1}(\hat{\mathbf{x}}) = \frac{\delta t}{2}\left[\dot{\mathbf{d}}^n(\hat{\mathbf{x}}) + \dot{\mathbf{d}}^{n-1}(\hat{\mathbf{x}})\right] \in \Gamma_{fsi}(0),
\tag{55}
$$

for IE-ALE update, or

$$
\hat{\mathbf{w}}_{int,k=1}^{n+1}(\hat{\mathbf{x}}) = \dot{\mathbf{d}}^n(\hat{\mathbf{x}}) \in \Gamma_{fsi}(0),
\tag{56}
$$

for CN-ALE update. Calculate $\sigma_{f\,k=1}^{n+1}$.

2. **Solid**: Solve for $\mathbf{d}_{k=1}^{n+1}$, $\dot{\mathbf{d}}_{k=1}^{n+1}$, $\ddot{\mathbf{d}}_{k=1}^{n+1}$ via Eqs. (26), (29) with $\sigma_{f\,k=1}^{n+1}$ on $\Gamma_{fsi}(t^{n+1})$.

Start FSI iterations in k from $k = 1$ until the FSI iteration convergence tolerance κ is reached:

3. **Fluid**: Calculate the new unrelaxed interface velocity as

$$
\bar{\mathbf{w}}_{int,k+1}^{n+1}(\hat{\mathbf{x}}) = \frac{\delta t}{2}\left[\dot{\mathbf{d}}_k^{n+1}(\hat{\mathbf{x}}) + \dot{\mathbf{d}}^n(\hat{\mathbf{x}})\right] \in \Gamma_{fsi}(0),
\tag{57}
$$

for IE-ALE update, or

$$
\bar{\mathbf{w}}_{int,k+1}^{n+1}(\hat{\mathbf{x}}) = \dot{\mathbf{d}}_k^{n+1}(\hat{\mathbf{x}}) \in \Gamma_{fsi}(0),
\tag{58}
$$

for CN-ALE update.

4. **Fluid**: Evaluate the FSI iteration convergence criteria κ_{i+1} based on the interface velocity

$$
\kappa_{i+1} = \left\|\bar{\mathbf{w}}_{int,k+1}^{n+1} - \hat{\mathbf{w}}_{int,k}^{n+1}\right\|_2 / \left\|\hat{\mathbf{w}}_{int,k}^{n+1}\right\|_2.
\tag{59}
$$

Exit the loop if κ_{i+1} is below a predefined threshold κ.

5. **Fluid**: Relax the interface velocity as

$$\hat{\mathbf{w}}_{int,k+1}^{n+1} = \omega_k \bar{\mathbf{w}}_{int,k+1}^{n+1} + (1 - \omega_k)\hat{\mathbf{w}}_{int,k}^{n+1}, \tag{60}$$

where

$$
\begin{aligned}
\omega_k &= -\omega_{k-1} \frac{\mathbf{R}_k \cdot \delta \mathbf{R}_k}{\delta \mathbf{R}_k \cdot \delta \mathbf{R}_k}, \\
\mathbf{R}_k &= \bar{\mathbf{w}}_{int,k+1}^{n+1} - \hat{\mathbf{w}}_{int,k}^{n+1}, \\
\delta \mathbf{R}_k &= \mathbf{R}_k - \mathbf{R}_{k-1},
\end{aligned}
\tag{61}
$$

with $\omega_1 = 0.75$.

6. **Fluid**: Solve for $\mathbf{u}_{k+1}^{n+1}$ and p_{k+1}^{n+1} via Eqs. (39), (40) (IE-ALE update), or (31), (32) (CN-ALE update), with the mesh velocity $\mathbf{w}_{k+1}^{n+1}$ calculated from Eq. (17), Eq. (38) using the relaxed interface velocity $\hat{\mathbf{w}}_{int,k+1}^{n+1}$ calculated in Step 5 from Eq. (60) as boundary conditions. Calculate $\sigma_{f\,k+1}^{n+1}$.

7. **Solid**: Solve for $\mathbf{d}_{k+1}^{n+1}$, $\dot{\mathbf{d}}_{k+1}^{n+1}$, $\ddot{\mathbf{d}}_{k+1}^{n+1}$ via Eqs. (26), (29) with $\sigma_{f\,k+1}^{n+1}$ on $\Gamma_{fsi}(t^{n+1})$.

   End FSI iterations.

The FSI iteration convergence tolerance κ is set to $\kappa = 10^{-5}$ in all the test cases presented in the current paper, apart from the tolerance sensitivity study in Sec. 5, for which it is varying.

3. Verification of h/p- and temporal convergence of component solvers

This section presents verification of h/p- and temporal convergence of the solid and fluid solvers, respectively, using known analytical solutions.

3.1. Solid solver: nonlinear elasticity

We present a verification of the developed nonlinear solid solver based on a St. Venant-Kirchhoff material model using both steady and unsteady nonlinear structural mechanics test cases.

3.1.1. Nonlinear elastostatics

For a nonlinear elastostatics problem, a cubic solid block with dimensions $[0, 1] \times [0, 1] \times [0, 1]$ is deformed by imposing a displacement field on all of the six faces as boundary conditions described as

$$
\begin{aligned}
d_x(X, Y, Z) &= A e^{aX} - A, \\
d_y(X, Y, Z) &= B e^{bY} - B, \\
d_z(X, Y, Z) &= 0,
\end{aligned}
\tag{62}
$$

where non-dimensional constants $A = B = 0.1$, $a = b = 1$, and X, Y, Z denote the undeformed geometry coordinates. The method of manufactured solutions is used, which takes displacements defined by Eq. (62) as the analytic solution, and introduces a body force field $\rho_s \mathbf{f}$ to the right-hand side of the elastostatics equations to satisfy the given solution. In the current case, the body force is determined by

$$
\begin{aligned}
\rho_s f_x(X, Y, Z) &= -C_1(2A\mu_s a^2 e^{aX} C_1 + Aa^2 \lambda_s e^{aX} C_1) - Aa^2 e^{aX}[\lambda_s(\frac{C_1^2}{2} + \frac{C_2^2}{2} - 1) + 2\mu_s(\frac{C_1^2}{2} - \frac{1}{2})], \\
\rho_s f_y(X, Y, Z) &= -C_2(2B\mu_s b^2 e^{bY} C_2 + Bb^2 \lambda_s e^{bY} C_2) - Bb^2 e^{bY}[\lambda_s(\frac{C_1^2}{2} + \frac{C_2^2}{2} - 1) + 2\mu_s(\frac{C_2^2}{2} - \frac{1}{2})], \\
\rho_s f_z(X, Y, Z) &= 0, \\
C_1 &= Aa e^{aX} + 1, \\
C_2 &= Bb e^{bY} + 1,
\end{aligned}
\tag{63}
$$

where the shear modulus μ_s and Lamé first parameter λ_s are calculated using a dimensionless Young's modulus $E = 1000$, Poisson's ratio $\nu_s = 0.3$ and density $\rho_s = 1$.

The original cubic geometry is uniformly discretized with spectral elements, using the same number of elements in X, Y and Z directions. The elements are therefore also cubic, with equal sizes in X, Y and Z directions in an undeformed configuration. The element size δX in the spatial convergence studies thus refers to an element size in any direction, and
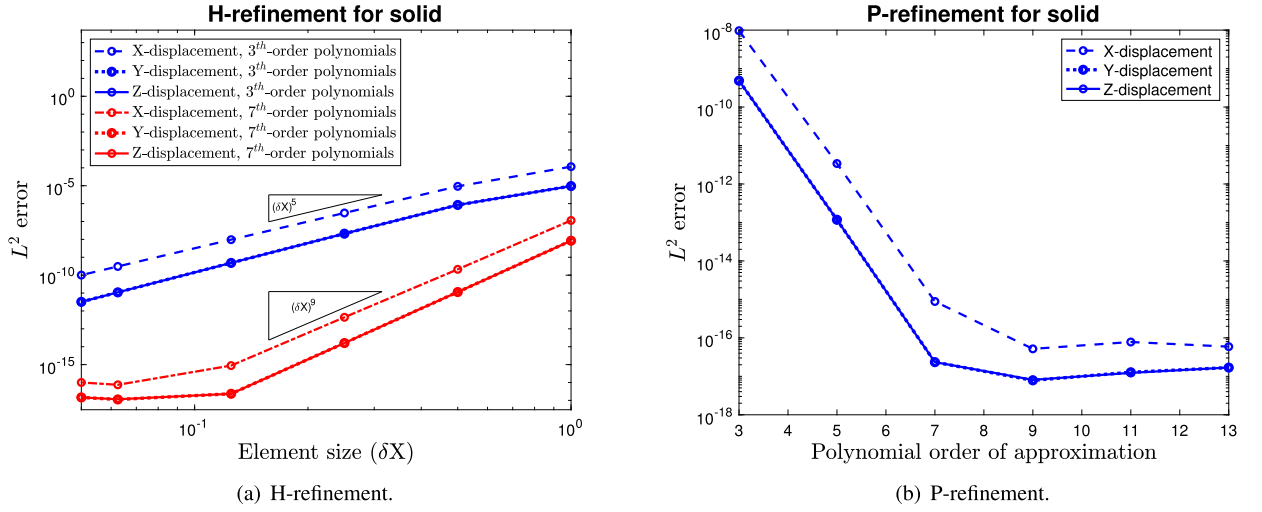
Fig. 1. Spatial convergence for a nonlinear elastostatics problem using nonlinear St. Venant-Kirchhoff material model. Element size refers to an undeformed configuration. P-refinement is performed with the element size $\delta X = 1/4$.

in regards to the original, undeformed, configuration. The spatial convergence for the nonlinear elastostatics problem using the L^2-error norm of the displacement defined as

$$L^2(\mathbf{d}) = \sqrt{\frac{\int_{\Omega_s}(\mathbf{d}_{ex} - \mathbf{d}_{comp})^2 \, d\Omega}{V_s}},\tag{64}$$

where, $\mathbf{d}_{comp}$ are the displacements obtained from the computations, $\mathbf{d}_{ex}$ are the corresponding exact values taken from Eq. (62), V_s is the volume of Ω_s in the undeformed configuration, is shown in Fig. 1. We observe a polynomial-order convergence with h-refinement, and a spectral convergence with p-refinement. Note that for h-refinement, the observed order of convergence is $O(\delta x^{N+2})$. The deviation of plots from an expected order of convergence starts when the errors due to spatial discretization drop below machine precision. Errors close to machine precision were observed previously in elastostatics problems with spectral element methods [19,43], which might be related to favorable properties of the matrix operators resulting from a discretization of the elastostatics equations.

3.1.2. Nonlinear elastodynamics

A nonlinear elastodynamics test case is performed to demonstrate the spatial and the temporal accuracy of the solid solver on the time-dependent problems. It shares the same geometry and material properties as the elastostatics test case described in Sec. 3.1.1. The analytic solution, however, is given by

$$d_x(X, Y, Z, t) = A\sin(aX)\sin(\pi t),$$
$$d_y(X, Y, Z, t) = d_z(X, Y, Z, t) = 0,\tag{65}$$

where the constants $A = 0.1$ and $a = 2$. Boundary conditions are, again, defined as Dirichlet boundary conditions on displacements, obtained by evaluating Eq. (65) at the domain boundary faces. For the time-dependent problem, we also need initial conditions that are given by

$$d_x(X, Y, Z, 0) = 0,$$
$$\dot{d}_x(X, Y, Z, 0) = A\pi\sin(aX),\tag{66}$$
$$\ddot{d}_x(X, Y, Z, 0) = 0,$$

and zero displacements, velocities and accelerations in Y and Z directions. Similarly, to enforce the displacement field defined by Eq. (65) as the analytic solution of the elastodynamics equation, Eq. (1), the body force is introduced as

$$\rho_s f_x(X, Y, Z, t) = 0.5Aa^2\sin(\pi t)\sin(aX)(2\mu_s + \lambda_s)[6Aa\sin(\pi t)\cos(aX)$$
$$+ 3A^2a^2\sin^2(\pi t)\cos^2(aX) + 2] - A\pi^2\sin(\pi t)\sin(aX),\tag{67}$$
$$\rho_s f_y(X, Y, Z, t) = \rho_s f_z(X, Y, Z, t) = 0.$$
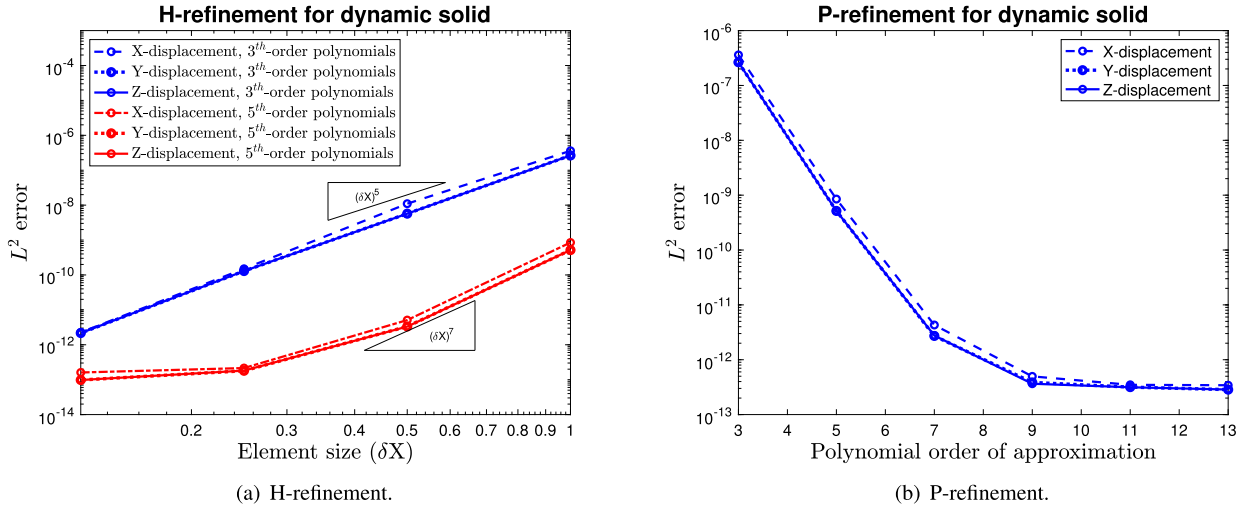
Fig. 2. Spatial convergence for a nonlinear elastodynamics problem using nonlinear St. Venant-Kirchhoff material model at time $t_f = 2$ using time step $\delta t = 10^{-5}$. Element size refers to an undeformed configuration. P-refinement is performed with the element size $\delta X = 1$.
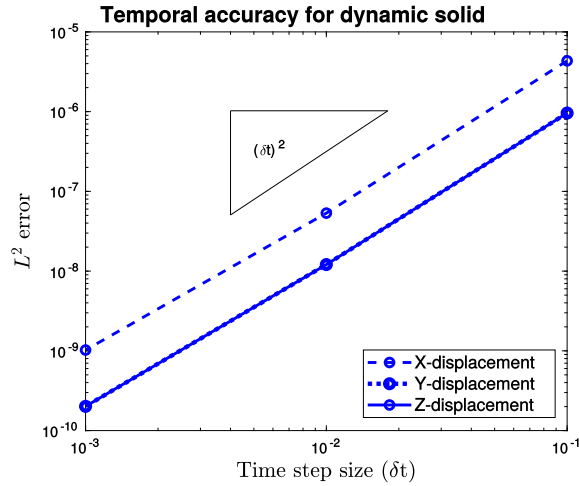

Fig. 3. Temporal convergence for an elastodynamics problem using nonlinear St. Venant-Kirchhoff material model at time $t_f = 2$. Element size $\delta X = 1/4$ with 7th-order polynomials. Element size refers to an undeformed configuration.

In the elastodynamics problem, the L^2 errors are defined as

$$L^2(\mathbf{d}) = \sqrt{\frac{\int_{\Omega_s} (\mathbf{d}_{ex} - \mathbf{d}_{comp})^2 \, d\Omega}{V_s}} \Big|_{t=t_f}, \tag{68}$$

where the exact value of displacements $\mathbf{d}_{ex}$ is taken from Eq. (65), and the notation $\big|_{t=t_f}$ signifies that the error is evaluated at the final time of the simulations t_f, where the final time is set to $t_f = 2$. Fig. 2 shows the results of a spatial refinement study for a nonlinear elastodynamics problem at the final time $t_f = 2$. Since a spatial error is significantly smaller compared to a temporal error in this problem, the time step size is set to a very small value of $\delta t = 10^{-5}$ to avoid an error interference. As with the static test, an order of convergence for the h-refinement tests is $O(\delta X^{N+2})$. The curve with higher-order polynomials starts to deviate from the expected slope at smaller element sizes due to the fact that the spatial discretization errors start interfering both with temporal and with machine precision errors. p-refinement plots show a clear spectral convergence all the way down to machine precision. Fig. 3 demonstrates the temporal convergence of the displacements at the same final time of $t_f = 2$. All three displacement components exhibit a second-order convergence in time, as expected. A temporal convergence study is performed using the mesh with the element size $\delta X = 1/4$ and 7th-order polynomials.

3.2. Fluid solver: convecting Walsh's eddies

Walsh [58] proves that if an initial condition $\mathbf{a}$ satisfies $\triangle \mathbf{a} = \lambda \mathbf{a}$ and $\nabla \cdot \mathbf{a} = 0$, then $\mathbf{u} = e^{\nu \lambda t}\mathbf{a}$ and $\nabla p = -\mathbf{u} \cdot \nabla \mathbf{u}$ would be a solution of the incompressible Navier-Stokes equations in an unbounded domain. Here, ν is the kinematic viscosity, and λ are the eigenvalues associated with the Walsh's eigenfunction solutions. Thus, a linear combination of several eigenfunctions could be used as an analytical exact solution for assessing spatial and temporal accuracy. To make the test case more interesting, a convecting version of Walsh's solution could be implemented by applying a convecting frame of reference to the original solution [58] by means of a coordinate transformation. Here, we use the same exact solution as in [57] that employs a coordinate transformation $x = \tilde{x} + c_x t$, $y = \tilde{y} + c_y t$, where (c_x, c_y) is the convecting velocity, $(\tilde{x}, \tilde{y})$ is the convecting frame of reference, where an original Walsh's solution is imposed, and (x, y) is the stationary frame of reference. The convecting Walsh's eddy solution, with the corresponding initial conditions given by the stream function

$$\psi(x, y, 0) = -\frac{1}{5}\cos(5x) - \frac{1}{5}\sin(5y) + \frac{1}{4}\sin(3x)\cos(4y) + c_x y - c_y x, \tag{69}$$

is then expressed as (see [57] for more details):

$$
\begin{aligned}
u_x(x, y, t) &= e^{-25\nu t}[-\cos(5\tilde{y}) + \cos(4\tilde{y})\sin(3\tilde{x})] + c_x, \\
u_y(x, y, t) &= e^{-25\nu t}[-\sin(5\tilde{x}) - \frac{3}{4}\cos(3\tilde{x})\sin(4\tilde{y})] + c_y, \\
p(x, y, t) &= \frac{1}{64}e^{-50\nu t}[-16 + 16\cos(6\tilde{x}) + 8\cos(8\tilde{x} - 4\tilde{y}) - 32\cos(2\tilde{x} - 4\tilde{y}) \\
&\quad + 9\cos(8\tilde{y}) - 8\cos(8\tilde{x} + 4\tilde{y}) + 32\cos(2\tilde{x} + 4\tilde{y}) - 4\sin(3\tilde{x} - 9\tilde{y}) \\
&\quad + 32\sin(5\tilde{x} - 5\tilde{y}) + 36\sin(3\tilde{x} - \tilde{y}) - 32\sin(5\tilde{x} + 5\tilde{y}) \\
&\quad + 36\sin(3\tilde{x} + \tilde{y}) - 4\sin(3\tilde{x} + 9\tilde{y})].
\end{aligned}
\tag{70}
$$

We use $(c_x, c_y) = (1, 0.3)$ for a convecting velocity, $\nu = 0.05$ for viscosity, and a square domain of $\Omega_f = [0, 2\pi] \times [0, 2\pi]$ for a geometry. The original square geometry is uniformly discretized with spectral elements, using the same number of elements in x and y directions. The elements are therefore also square, with equal sizes in x and y directions in an undeformed configuration. The element size δX in the spatial convergence studies thus refers to an element size in any direction, and in regards to the original, undeformed, configuration. Boundary conditions at the edges of Ω_f are set up as Dirichlet conditions on velocity evaluated from Eq. (70), while pressure boundary conditions in the current $P_N - P_{N-2}$ formulation are not required, and are evaluated internally using homogeneous Neumann boundary conditions [9].

To test the performance of the developed ALE fluid solver on deformable meshes, a domain deformation shown in Fig. 4 based on undeformed mesh coordinates X and Y is imposed as

$$
\begin{aligned}
w_x(X, Y, t) &= \frac{1.2\pi}{5}\sin(X)\sin(Y)\cos(\frac{2\pi}{5}t), \\
w_y(X, Y, t) &= \frac{2.4\pi}{5}\sin(X)\sin(Y)\cos(\frac{4\pi}{5}t).
\end{aligned}
\tag{71}
$$

Note, since ALE equations (10), (11) transform back to the original Navier-Stokes equations in a stationary domain when the ALE derivative $\frac{\partial}{\partial t}\big|_{\hat{\mathbf{x}}}$ is converted back to the Eulerian derivative $\frac{\partial}{\partial t}\big|_{\mathbf{x}}$, the flow solution in both stationary and deformed domains is the same, as long as the domain deformation does not influence the flow through a modification of the boundary conditions (as would be the case if actual moving or deforming objects were present). Since, in the current case, the mesh movement is entirely "virtual" (no actual solid surfaces are moving), the flow solution given by Eq. (70) still holds on a deforming domain.

The spatial and temporal convergence for both velocity and pressure fields is investigated through an L^2 error norm defined as

$$
\begin{aligned}
L^2(\mathbf{u}) &= \sqrt{\frac{\int_{\Omega_f}(\mathbf{u}_{ex} - \mathbf{u}_{comp})^2 \, d\Omega}{V_f}}\Big|_{t=t_f}, \\
L^2(p) &= \sqrt{\frac{\int_{\Omega_f}(p_{ex} - p_{comp})^2 \, d\Omega}{V_f}}\Big|_{t=t_f},
\end{aligned}
\tag{72}
$$

where V_f is the volume of the domain Ω_f, subscript $comp$ is the result from the computations, ex is the analytical value that refers to Eq. (70) in this case, and the notation $\big|_{t=t_f}$ signifies that the error is evaluated at the final time of the simulations t_f.

(a) Element size $\delta X = 2\pi/8$ with 5th-order polynomials.

(b) Element size $\delta X = 2\pi/16$ with 17th-order polynomials.
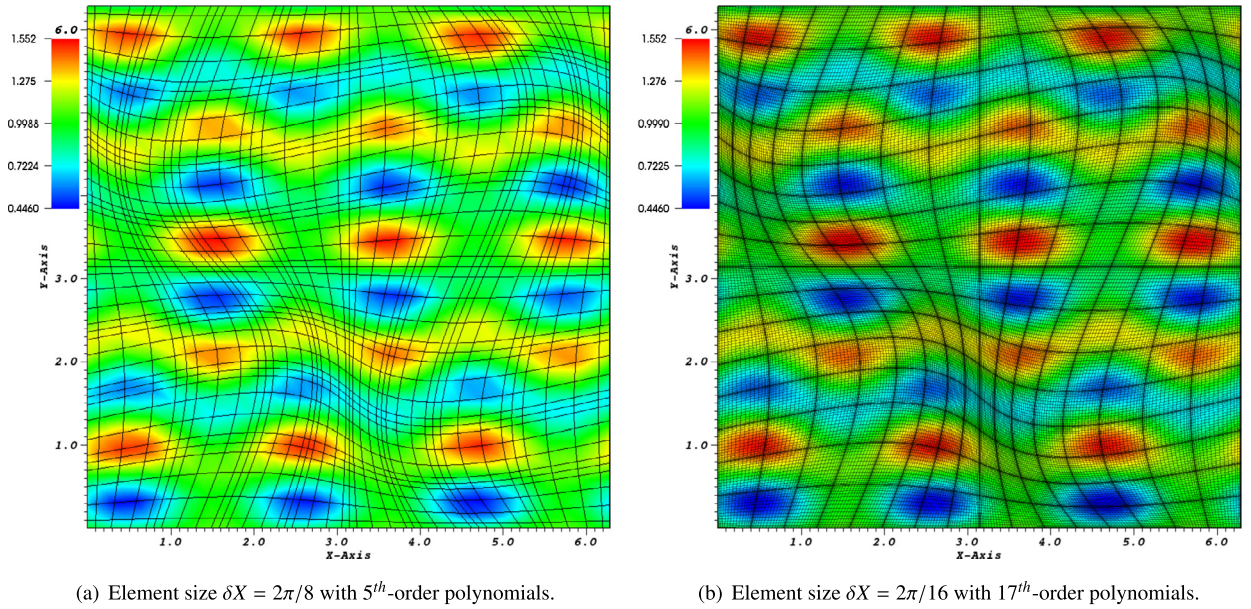
Fig. 4. Mesh deformation and the *x*-velocity solution for the convecting Walsh's eddies case at $t = 1$. Element size refers to an undeformed configuration.
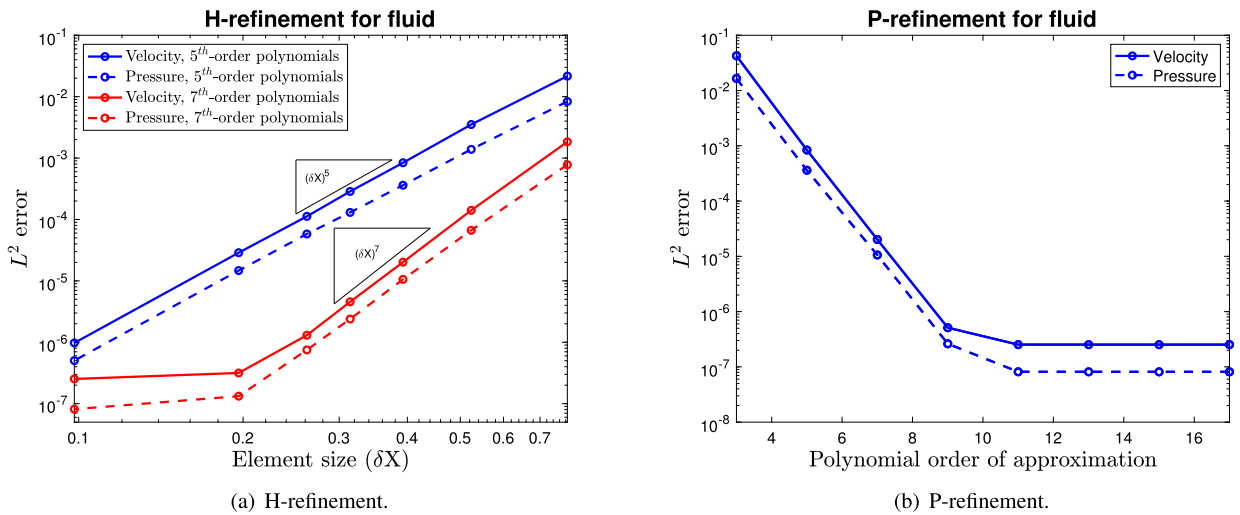

(a) H-refinement.

(b) P-refinement.

Fig. 5. Spatial refinement for the convecting Walsh's eddies case at time $t_f = 1$ using time step $\delta t = 10^{-4}$. Element size refers to an undeformed configuration. P-refinement is performed with the element size $\delta X = 2\pi/16$.

Spatial convergence study is performed with time step $\delta t = 10^{-4}$. Fig. 5(a) shows the L^2 error norm convergence of velocity and pressure fields with regard to the varying element sizes δX by 5th and 7th order polynomials. The convergence rates of velocity and pressure fields demonstrate the expected $O(\delta X^N)$ polynomial order of convergence. The *p*-refinement plot shown in Fig. 5(b) confirms a spectral convergence for both velocity and pressure fields. Both plots confirm the expected spectral-element convergence rates on deforming meshes. The deviation of plots from an expected order of convergence starts when the errors due to spatial discretization drop below a temporal error of about $O(\delta t^2) \sim 10^{-8} - 10^{-7}$ as expected.

The temporal convergence shown in Fig. 6 contains the results at $t_f = 5$ from BDF2 background temporal scheme with three options for the interface update: 1) IE-ALE interface update with GCL, 2) IE-ALE interface update with no GCL, 3) CN-ALE interface update with no GCL. A temporal convergence study is performed using the mesh with the element size $\delta X = 2\pi/16$ and 13th-order polynomials. As expected, BDF2 with IE-ALE interface update does not achieve second order temporal accuracy without GCL, since the geometry is updated linearly [46]. The two other schemes show the expected second-order temporal convergence rates on deforming meshes.
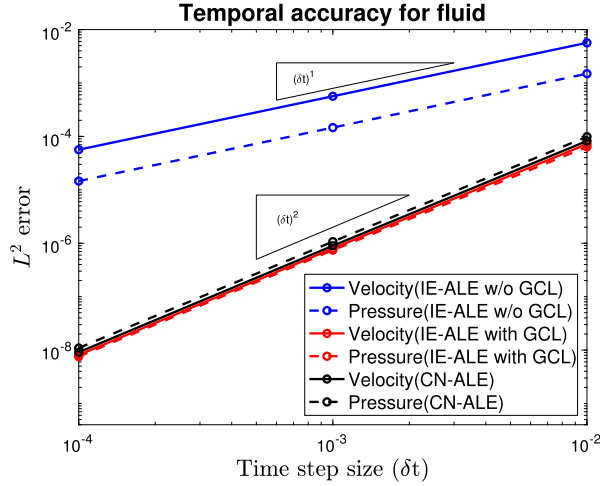
Fig. 6. Temporal convergence for the convecting Walsh's eddies case at time $t_f = 5$. Element size $\delta X = 2\pi/16$ with 13th-order polynomials. Element size refers to an undeformed configuration.
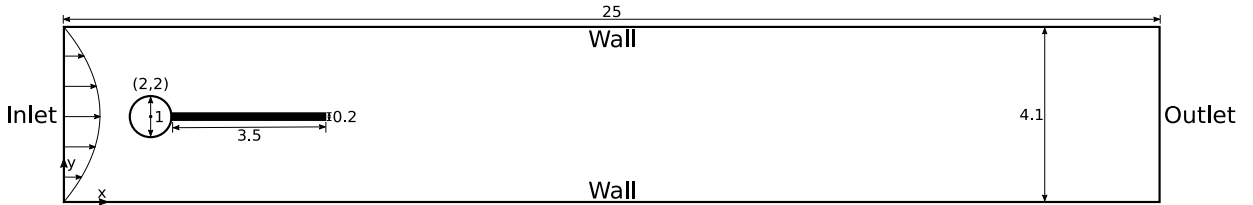

Fig. 7. Non-dimensional 2D FSI benchmark geometry following Ref. [33].

4. Verification of the fluid-structure interaction solver against available benchmark solutions

This section concerns with a verification of the developed high-order fluid-structure interaction solver against available numerical benchmarks solutions. We start with a two-dimensional test case proposed by Turek and Hron [33], and then proceed to a three-dimensional pressure wave propagation test case considered in Refs. [36,38]. In all the test cases presented below, fluid and solid spectral-element meshes are conforming, and the same degree of the polynomial approximation is used for both the fluid and the solid solvers, i.e. the information between the corresponding fluid and solid nodes at the interfaces can be directly exchanged, without the need for an interpolation.

4.1. 2D Turek-Hron [33] FSI benchmark

A common fluid-structure interaction benchmark, versus which a performance of the fluid-structure interaction codes is often assessed [15,16,59], involves a two-dimensional problem proposed by Turek and Hron [33], which consists of an interaction of an incompressible fluid with a geometrically nonlinear structure, where a fluid flowing over a rigid cylinder excites a flexible cantilever beam attached to a cylinder, as shown in a geometrical setup in Fig. 7, where all geometrical parameters have been non-dimensionalized by the cylinder diameter. The fluid solver boundary conditions are set as a parabolic velocity inlet given by Eq. (73) below; a constant-pressure derivative-free outlet; and no-slip, rigid and stationary top, bottom and cylinder walls. A flexible elastic solid bar with a curved left side for a no-gap connection is fully attached to the cylinder. The boundary conditions between the fluid and the flexible elastic bar are the FSI interface conditions defined by Eqs. (23), (24).

Following [33], the inlet flow velocity profile is prescribed as

$$
u_x = \begin{cases} 1.5\mathrm{U}\,\dfrac{y(4.1-y)}{(4.1/2)^2}\,\dfrac{[1-\cos(\pi t/t_u)]}{2} & 0 \le t < t_u, \\[4mm] 1.5\mathrm{U}\,\dfrac{y(4.1-y)}{(4.1/2)^2} & t \ge t_u, \end{cases} \tag{73}
$$

where a nonlinear ramping function is applied to an inlet velocity over a time period t_u to alleviate the numerical issues associated with an abrupt start-up motion.

(a) *X*-displacement comparison for CSM3 test.

(b) *Y*-displacement comparison for CSM3 test.
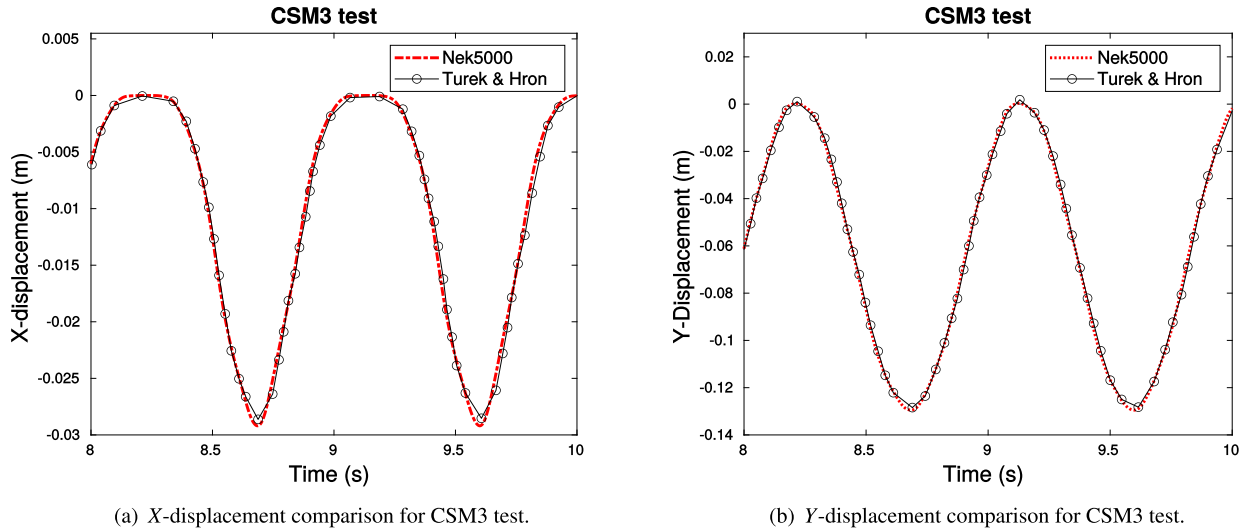
Fig. 8. CSM3 test case comparison for the solid solver with the results of the FSI benchmark [33]. Displacements are for the point located at the rightmost tip of the bar along the centerline.

A nonlinear St. Venant-Kirchoff structural dynamics equation, Eq. (1), is solved within the flexible bar, but not within the rigid cylinder, and the solid boundary conditions for the bar are set as the zero displacements at the left curved side, and FSI interface boundary conditions (23) and (24), at all the other three sides of the bar interacting with the fluid. The fluid mesh contains a total of 760 spectral elements, and the solid mesh contains 34. The solution for all the test cases is obtained with the 6th order polynomial approximation.

In this paper, we compare the results of Ref. [33] with the current spectral-element results for the solid-only, fluid-only, and the FSI test cases, termed as CSM3, CFD3 and FSI3 in [33]. In the CSM3 test case, the geometry of the problem contains only the solid bar with the left side fixed, and an additional gravity force. In the CSM3 test, the original, non-rescaled, geometry by [33] is used, with the non-dimensional structure properties set as the solid density $\rho_s = 1000$, Poisson's ratio $\nu_s = 0.4$, Young's modulus $E = 1400000$, and a gravity force $f_y = -2$.

For the CFD3 and FSI3 test cases, the geometry is used as shown in Fig. 7, non-dimensionalized by the cylinder diameter, and the other non-dimensional parameters are set as $t_u = 2$, $U = 20$, $\rho_f = \rho_s = 1$ as fluid and solid density, fluid viscosity $\mu = 0.1$, Young's modulus for the solid is $E = 560000$, Poisson's ratio is $\nu_s = 0.4$, and the outflow pressure is set to a reference value of 0. In the CFD3 case, the geometry is as in Fig. 7, but the solid bar is kept stationary. In FSI3, a complete fluid-structure interaction of the presented geometry is studied.

The CSM3 results documenting the temporal history of X and Y displacements of the point located at the rightmost tip of the bar along the centerline for Nek5000 as compared to Ref. [33] are shown in Fig. 8. For the CFD3 test case, the total lift and drag over the cylinder and the bar are compared in Fig. 9. For both test cases, the results shown in Fig. 8 and Fig. 9 confirm excellent agreement with Ref. [33].

The visualization of the streamwise velocity field for the FSI3 test case computed by Nek5000 is presented in Fig. 10 for two selected times of $t = 4.475$ and $t = 4.575$. A corresponding mesh deformation pattern, zoomed in around the solid structure is shown in Fig. 11. The comparison of both the total lift and drag, as well as the streamwise and vertical displacement of the rightmost tip of the bar along the centerline, for the FSI3 test case, are shown in Fig. 12 and Fig. 13. Again, an excellent agreement between the current computations and Turek and Hron [33] results is observed, with only 38,906 total degrees of freedom in the current mesh.

4.2. 3D FSI pressure wave propagation benchmark

In this section, we compare the results of our three-dimensional spectral-element FSI implementation with the previous numerical solutions using a 3D FSI test case that considers a pressure wave propagation in a flexible pipe proposed in [36] and later studied in [38]. The geometry consists of a cylindrical pipe with a flexible thin wall of a thickness $d = 0.1D$, where D is the inner diameter of the pipe. The pipe has a length of $5D$ and is filled with an incompressible fluid. The three-dimensional pipe geometry is presented in Fig. 14(a), and a spectral-element mesh for the fluid and solid is shown in Fig. 14(b), where the blue color corresponds to the fluid mesh, and the green color to the solid mesh. The fluid mesh contains 32 elements along the circumference, two layers of elements between the radial distance of 0.45 to 0.5 (normalized with the pipe diameter), one layer of elements between the radial distance of $[0.4, 0.45]$, and the core of the cross-sectional circular mesh consists of approximately uniform quadrilateral elements with the average element size of ~ 0.08. The fluid mesh has a total of 224 elements inside the cylindrical cross-section, and 40 equally spaced elements in the streamwise
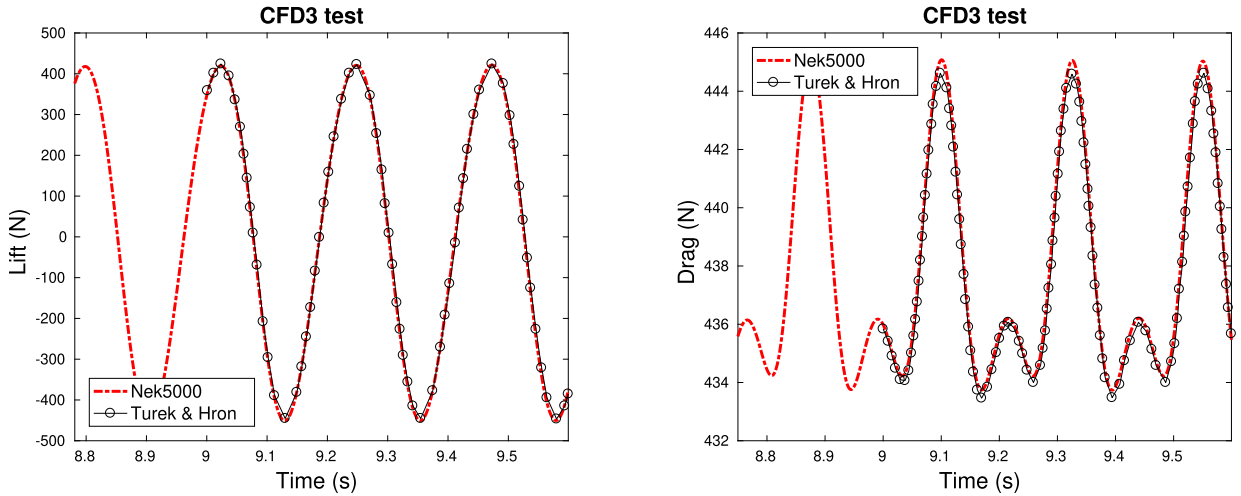
(a) Lift comparison for CFD3 test.

(b) Drag comparison for CFD3 test.

Fig. 9. CFD3 test case comparison for the fluid solver with the results of the FSI benchmark [33].
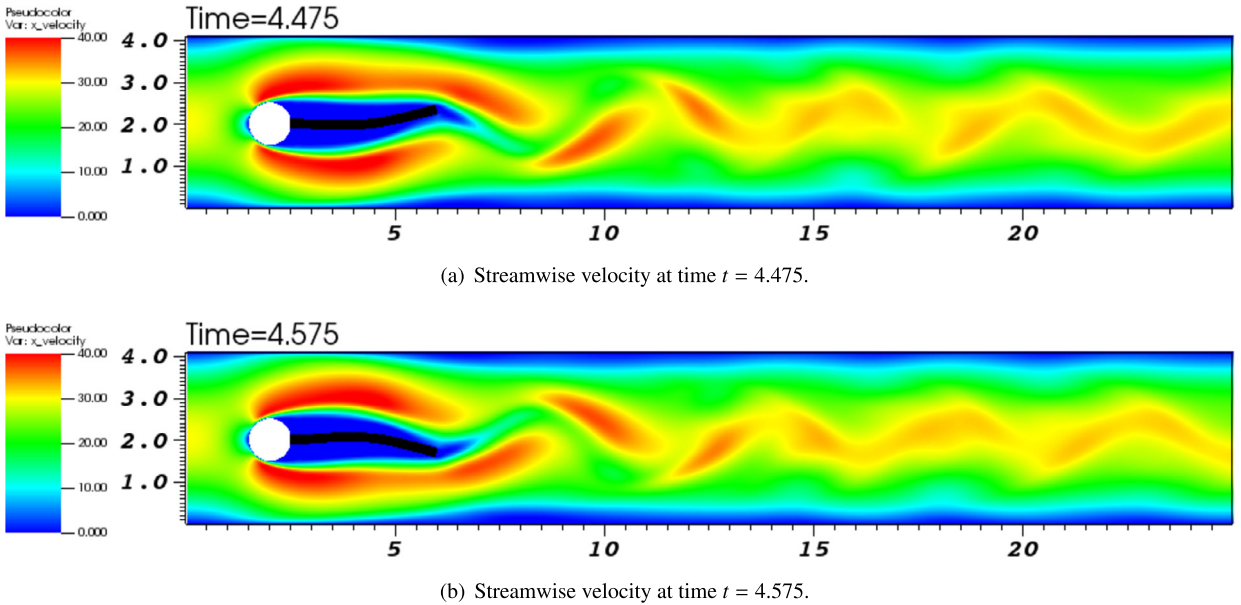

(a) Streamwise velocity at time $t = 4.475$.

(b) Streamwise velocity at time $t = 4.575$.

**Fig. 10.** Visualization of streamwise velocity for FSI3 test case.

direction. The solid is discretized with one layer of elements across the wall thickness, while the element distribution along the circumferential and streamwise directions matches that of the fluid. The fluid is assumed to be incompressible, as before, and the solid is discretized with a nonlinear St. Venant-Kirchoff material model. In the current test case, the fluid has the non-dimensional density $\rho_f = 1$ and viscosity $\mu = 0.035$. The solid has a density $\rho_s = 1.2$, Young's modulus $E = 3 \times 10^6$ and a Poisson's ratio $\nu_s = 0.3$. Both fluid and solid parameters, as well as the initial and boundary conditions described below, match the parameters of Refs. [36,38]. The pipe flow in the current test case is driven by an inlet pressure, the outlet pressure is kept at zero, and the rest of the fluid boundary is the FSI interface. For the solid, the inner surface is interacting with the fluid through the FSI boundary conditions, the outer surface is stress-free, and the structure is clamped at the inlet and outlet.

To initialize the pressure wave propagation benchmark, the fluid, originally at rest, is disturbed by a sudden inlet pressure impulse of the magnitude of 1.3332×10^4 applied for the time period $[0, 0.005]$, after which the inlet pressure goes back to zero. This pressure impulse sends a pressure wave into the domain, which propagates downstream and causes the deflection of the pipe surface as shown in Fig. 15. In the current setup, the z axis is in the streamwise direction, while x and y axes are in the pipe cross-sectional plane. In the current test case, the maximum fluid streamwise velocity achieved is $U_{max} = 28$,
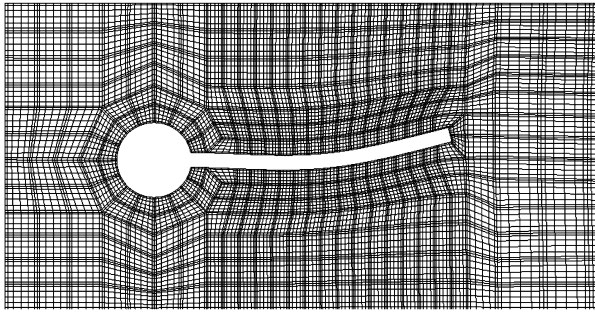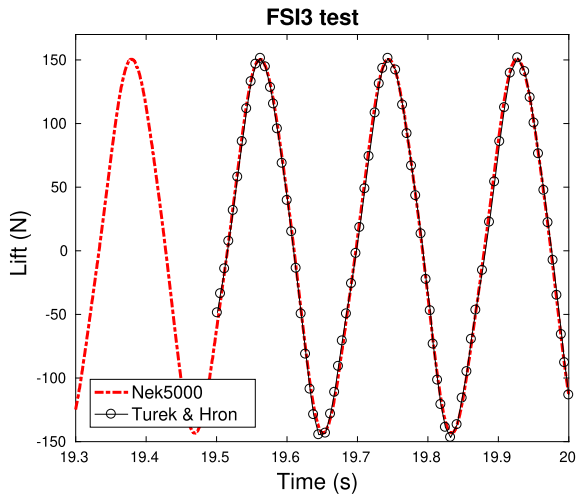
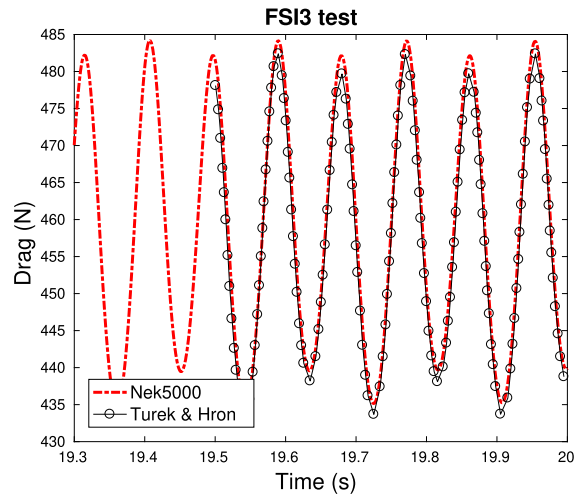(a) Mesh deformation visualization for FSI3 test at time $t = 4.475$.
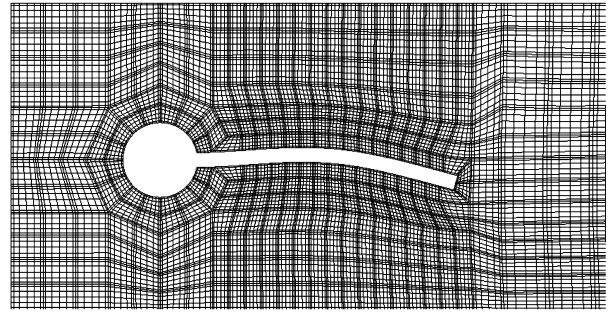
(b) Mesh deformation visualization for FSI3 test at time $t = 4.575$.

Fig. 11. FSI3 test case mesh deformation visualization with 6th-order polynomials.
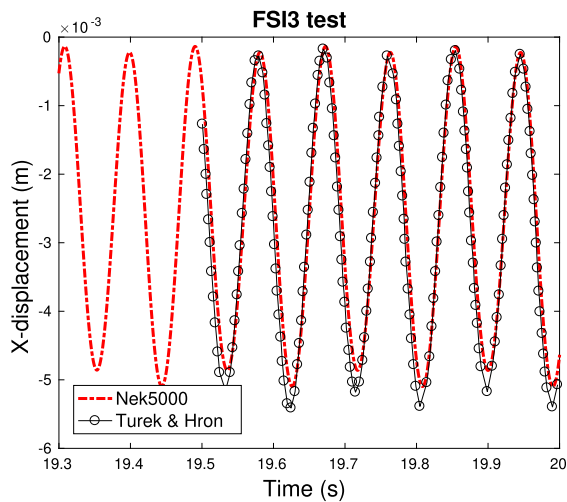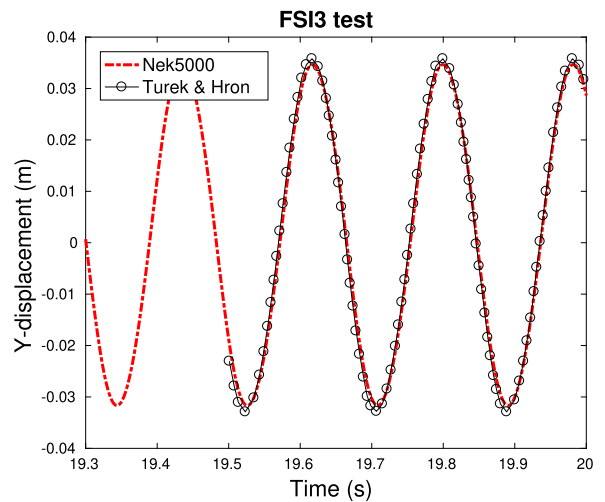

(a) Lift comparison for FSI3 test.

(b) Drag comparison for FSI3 test.

Fig. 12. FSI3 test case comparison with the results of the FSI benchmark [33].
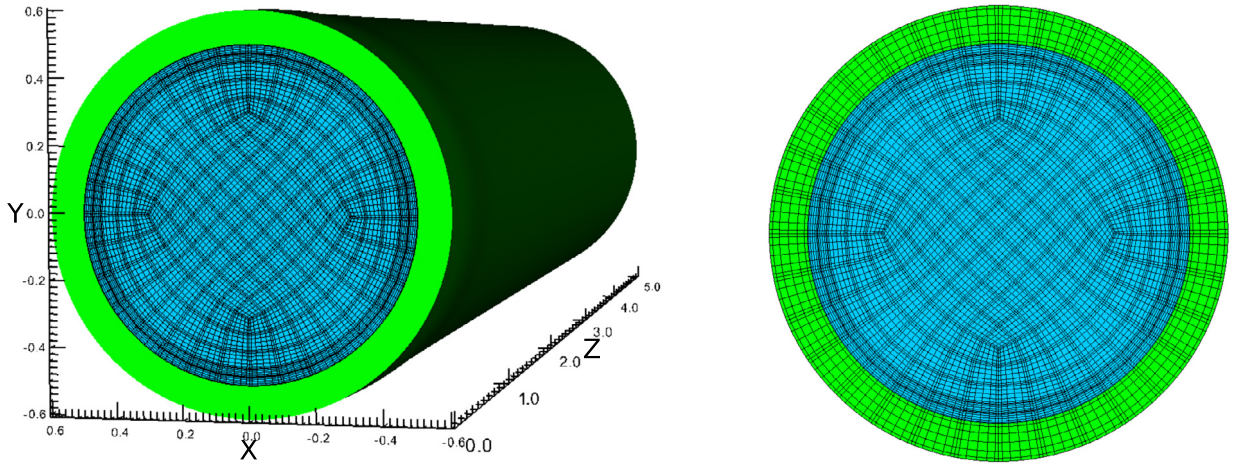

(a) X-displacement comparison for FSI3 test.

(b) Y-displacement comparison for FSI3 test.

Fig. 13. FSI3 test case comparison with the results of the FSI benchmark [33]. Displacements are for the point located at the rightmost tip of the bar along the centerline.

(a) Pipe geometry, mesh and a pressure field visualization computed with 6th-order polynomials.

(b) A close-up view of the spectral-element mesh across the pipe cross-section. Blue color corresponds to the fluid mesh, and green – to the solid mesh.

Fig. 14. 3D pipe geometry and the computational mesh for the SEM simulations of the 3D FSI pressure wave propagation benchmark.
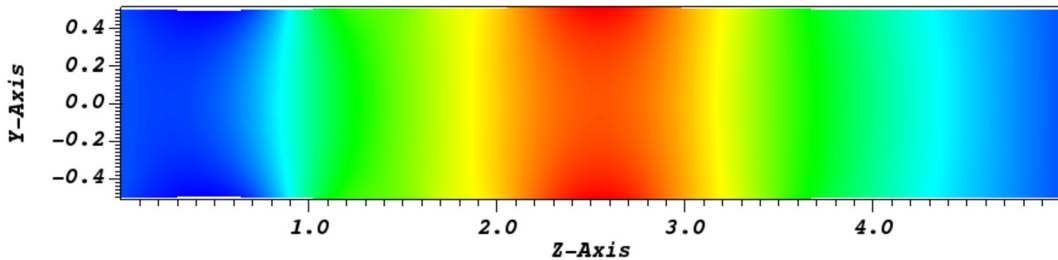
Fig. 15. Visualization of the pressure field and a pipe deflection in the streamwise-radial plane at time $t = 0.0075$ for the 3D FSI pressure wave propagation benchmark. Solution is computed with 6th-order polynomials both for the fluid and for the solid.

which gives a Reynolds number estimate of $Re_{max} = U_{max}D/\nu = 800$, based on the pipe diameter. This ensures that the flow stays in a laminar regime, and the pipe deformation is axisymmetric. Following [38], we track a temporal evolution of the point with coordinates $(X, Y, Z) = (0.5, 0, 2.5)$ in the undeformed configuration, which corresponds to a point at the fluid-structure interface in the middle of the tube. Again, since the motion is axisymmetric, any interface point with $Z = 2.5$ should give the same results.

The simulations are performed with 4th and 6th-order polynomials and time steps $\delta t = 10^{-4}$ and $\delta t = 4.4721 \times 10^{-5}$. The temporal evolution of the displacement of the middle point of the pipe FSI interface is compared with the results of the implicit method of Fernández et al. [38], which uses second-order accurate in space finite element (FEM) discretization, in Fig. 16. The interface displacement occurs both in the radial and in the streamwise directions, so that the displacement magnitude is compared. We first note that Nek5000 results with $p = 4$ and $p = 6$ are nearly identical, which testifies of an adequate spatial resolution for this problem. While the agreement with the results of Fernández et al. [38] is generally very good, slight differences are noted. We first remark that both the current results and the results of Ref. [38] are sensitive to the time step value, with a consistent trend of an upward shift of the peak at smaller time steps. We also note a time lag of the peak in SEM versus FEM, testifying that the spatial discretization also affects the temporal dynamics. Sensitivities to the time step and the influence of spatial discretization on the time shift in a structure response in the FSI problems will be further discussed in Sec. 5. While the 2D Turek and Hron [33] FSI benchmark was studied extensively, results for this 3D FSI benchmark are scarce. More numerical solutions are needed to establish the uncertainty bounds on the results produced so far by these two numerical methods, FEM by [38] and the current SEM.

5. New proposed 3D FSI benchmark: flow in a compliant wall channel

5.1. Problem formulation

5.1.1. Geometry

In this section, we present a new three-dimensional benchmark for studying a fluid-structure interaction problem, which uses consistent initial and boundary conditions, continuous both in space and time, and is quite simple to implement. The
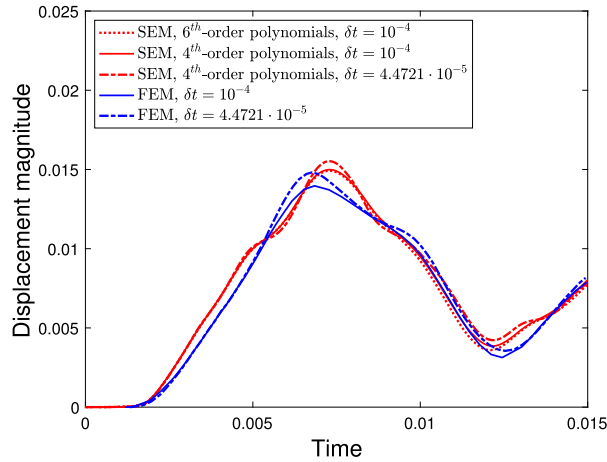
Fig. 16. Comparison of the magnitude of midpoint displacement versus time with Fernández et al. [38] for the 3D FSI pressure wave propagation benchmark. Fernández et al. [38] results are from their implicit coupling method.

benchmark is inspired by a physical problem of a fluid flow in a channel interacting with a compliant wall, which has potential applications in flow control related to a delay of a laminar-to-turbulent transition [5,6], as well as skin friction drag reduction [7].

The proposed benchmark is studied in this section to verify the h/p- and temporal convergence of a high-order spectral element solver on a globally-coupled FSI problem using self-convergence tests. The effect of the solver tolerances on the numerical errors in the FSI setting is also discussed.

The geometry for the proposed FSI benchmark consists of a rectilinear channel flow domain of the dimensions $[0, 6] \times [-1, 1] \times [-1, 1]$ filled with incompressible fluid (all distances are normalized with the channel half-width), and a flexible solid layer with dimensions $[0, 6] \times [1, 1.2] \times [-1, 1]$ added on top of the fluid domain. Note, in this setting, only one (top) channel wall is elastic, while the other (bottom) wall is rigid, a configuration typical in previous studies of a compliant wall channel [40,41]. The bottom rigid wall is thus not modeled by a solid solver, but rather represented by the no-slip boundary conditions in the fluid domain. The other boundary conditions for the fluid are periodic in a spanwise direction, fluid-structure interface for the top compliant wall, inlet velocity boundary conditions, and outflow boundary conditions with a constant pressure set to zero at the outlet. The solid domain added to the top of the fluid domain also has periodic boundary conditions in a spanwise direction, it is clamped at the inlet and outlet (zero displacements), its top surface is stress-free, and its bottom surface that interacts with the fluid has the FSI interface boundary condition.

The initial condition for the fluid flow is a laminar parabolic velocity profile $(u_x, u_y, u_z) = (U(y), 0, 0)$, where the non-dimensional velocity profile is specified as

$$U(y) = 0.15(1 - y^2), \tag{74}$$

while the solid starts at rest (zero displacements, velocities, and accelerations). The non-dimensional material properties for the fluid are $\rho_f = 1$, $\mu = 0.0001$ (corresponding to a flow Reynolds number of 1500 based on a channel half-width and an unperturbed centerline velocity), and for the solid the parameters are $\rho_s = 5$, $\nu_s = 0.3$, $E = 300$, with a St. Venant Kirchhoff material model used to model nonlinearly-elastic solid behavior. The unsteady interaction between the fluid and the structure is initiated by sending a transient velocity perturbation through the inlet into the flow domain, in the form of

$$u_x(0, y, z, t) = \begin{cases} U(y) + u'(y, z, t), & 0 \le t < t_u, \\ U(y) & t \ge t_u, \end{cases} \tag{75}$$

where the perturbation $u'(y, z, t)$ is given by

$$u'(y, z, t) = 0.075(1 - y^2)\frac{1 - \cos(2\pi t)/t_u}{2}, \tag{76}$$

which corresponds to an unsteady velocity perturbation with a peak amplitude of 0.0075 (5% of the undisturbed centerline velocity). This perturbation, also in a form of a parabolic profile consistent with the fluid domain boundary conditions, is added to the undisturbed flow profile $U(y)$ given by Eq. (74) for a duration of a time period $t_u = 2$. The perturbation is designed to gradually increase while $t \in [0, t_u/2]$ and then gradually decrease until zero at $t = t_u$, after which the perturbation is turned off, and the flow inlet velocity assumes its undisturbed value. The simulations are run from the beginning of the transient ($t = 0$) until the final time of $t_f = 25$. A three-dimensional view of the simulated flow velocity and the solid deformation at a time $t = 20$ is provided in Fig. 18. The temporal series of the midpoint wall vertical displacement
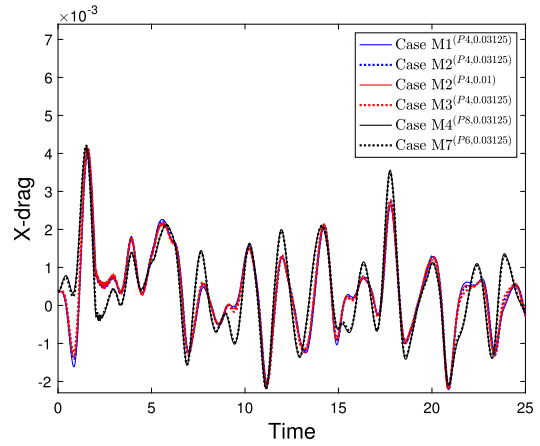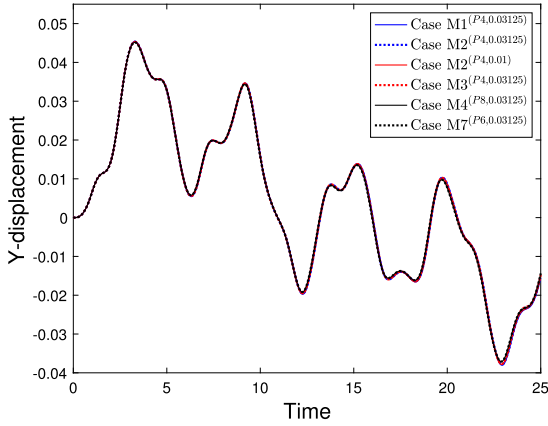
(a) Midpoint wall vertical displacement for the baseline (M) meshes.

(b) Total flow drag on the compliant wall for the baseline (M) meshes.
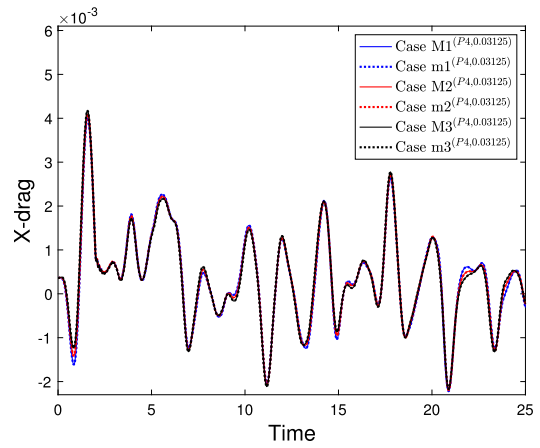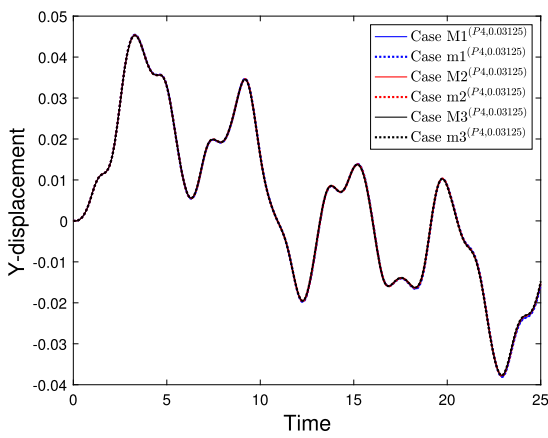
(c) Midpoint wall vertical displacement. Comparison of meshes with one vertical layer (m) and two vertical layers (M) of solid elements.

(d) Total flow drag on the compliant wall. Comparison of meshes with one vertical layer (m) and two vertical layers (M) of solid elements.

Fig. 17. Temporal series of the midpoint wall vertical displacement and the total flow drag (pressure and viscous drag) on the compliant wall for different meshes.
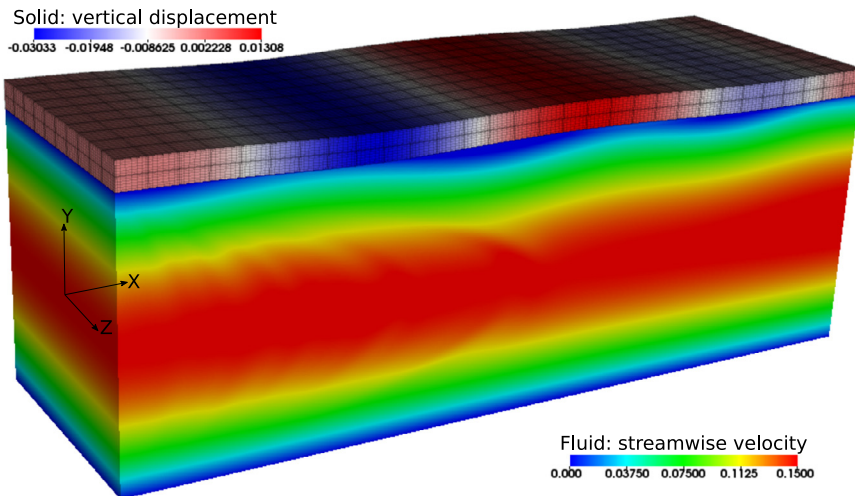
Fig. 18. The fluid flow and the solid deformation at a time $t = 20$ for the proposed compliant wall channel 3D FSI benchmark using the mesh $M4^{(P8,0.03125)}$, see Table 1. Fluid field: streamwise velocity; solid field: vertical displacement.

Table 1

Meshes used for the self-convergence studies in the proposed compliant wall channel 3D FSI benchmark.

Mesh level	M1	M2	M3	M4	M5	M6	M7
Element size, δY, solid	1/10	1/10	1/10	1/10	1/10	1/10	1/10
Element size, δX, fluid and solid, all other directions	1/2	1/3	1/4	1/5	1/6	1/7	1/8
Total number of elements (fluid and solid)	288	864	1920	3600	6048	9408	13824

Table 2

Meshes with one vertical layer of solid elements.

Mesh level	m1	m2	m3
Element size, δY, solid	1/5	1/5	1/5
Element size, δX, fluid and solid, all other directions	1/2	1/3	1/4
Total number of elements (fluid and solid)	240	756	1728

Table 3

Test meshes and a reference mesh for each type of the refinement studies performed in the proposed compliant wall channel 3D FSI benchmark.

Type of study	Mesh level	Polynomial order	Time step, δt	Tolerances, $\kappa_s, \kappa_f, \kappa$	Reference mesh
H-refinement	$M1 - M4$	P4	0.03125	$10^{-12}, 10^{-6}, 10^{-5}$	$M5^{(P4, 0.03125)}$
P-refinement	M4	P4, P6, P8	0.03125	$10^{-12}, 10^{-6}, 10^{-5}$	$M7^{(P6, 0.03125)}$
Time-refinement	M2	P4	0.03125, 0.0625, 0.125	$10^{-12}, 10^{-6}, 10^{-5}$	$M2^{(P4, 0.01)}$

and the flow drag on the compliant wall (fluid force in a streamwise direction, see Eq. (77)), using the series of meshes described below, are shown in Fig. 17. Fig. 17 and Fig. 18 demonstrate that although the original perturbation is switched off at a time $t = 2$, an unsteady cycle of the fluid structure interaction persists far beyond the time during which the original perturbation is active.

5.1.2. Description of meshes

In this section, we perform a spatial and a temporal refinement study using a series of meshes, $M1 - M7$. For the meshes $M1 - M7$, the number of solid elements in the y direction is fixed at two (size of $\delta Y = 1/10$ in wall-normal direction). We also add three additional meshes, $m1$, $m2$ and $m3$, with one vertical layer of solid elements instead of two, to check a spatial refinement of the solid, see Table 2. The size of the elements in all other directions (x and z for the solid, and x, y and z for the fluid) is the same within each mesh level, and is uniformly refined across the meshes, following a relation $\delta(Mk) = 1/(k+1)$, $\delta(mk) = 1/(k+1)$. As before, the element size δX refers to an element size in any direction for the fluid, and to either x or z direction for the solid (while $\delta Y = 1/10$ or $\delta Y = 1/5$ for the solid meshes), and in regards to an original, undeformed, configuration. Table 1 and Table 2 show the corresponding element sizes and the total number of elements (in fluid and solid meshes combined) for all the meshes simulated.

In a series of verification studies presented below, including h-refinement, p-refinement and temporal refinement, the meshes from Table 1 are used with a varying polynomial order and time step of the simulation. To keep the notation clear, we define the mesh at a level k with the polynomial order p and a time step δt as $Mk^{(Pp, \delta t)}$. For example, the mesh M2 using 4th order polynomials and a time step $\delta t = 0.03125$ is denoted as $M2^{(P4, 0.03125)}$. Furthermore, for a consistent refinement study, the reference solution is taken from a mesh that has a highest level of refinement in a variable with respect to which the refinement is studied. Table 3 gives a list of the test meshes and a mesh used for a reference solution for each type of the refinement studies performed. The tolerances in the spatial and temporal refinement studies are set to their baseline values of $\kappa_s = 10^{-12}$, $\kappa_f = 10^{-6}$, $\kappa = 10^{-5}$ in all the test meshes and the reference mesh, as shown in Table 3, while they vary in the tolerance sensitivity study as described below.

5.1.3. Error metrics

To evaluate the performance of the coupled solver and the errors of approximation pertinent to an unsteady fluid-structure interaction problem, we monitor the time-dependent errors of the two relevant quantities: 1) vertical displacement of the midpoint of the FSI interface, $d_y (X_m, Y_m, Z_m, t)$, where $(X_m, Y_m, Z_m) = (3, 1, 0)$ in the undeformed configuration, 2) the flow drag at the FSI interface defined as the integral of the x-component of the local fluid force,

$$F_d(t) = - \int_{\Gamma_{fsi}(t)} (\sigma_f \vec{n}_f) \cdot \vec{i} \, d\Gamma, \tag{77}$$

where σ_f is the Cauchy stress tensor of the fluid defined by Eq. (25), $\vec{n}_f$ is the outward-pointing unit normal vector at the FSI interface, $\vec{i}$ is the unit vector in a streamwise direction. Since the fluid Cauchy stress tensor consists of the pressure and viscous components, pressure and viscous drag can be defined, correspondingly, as
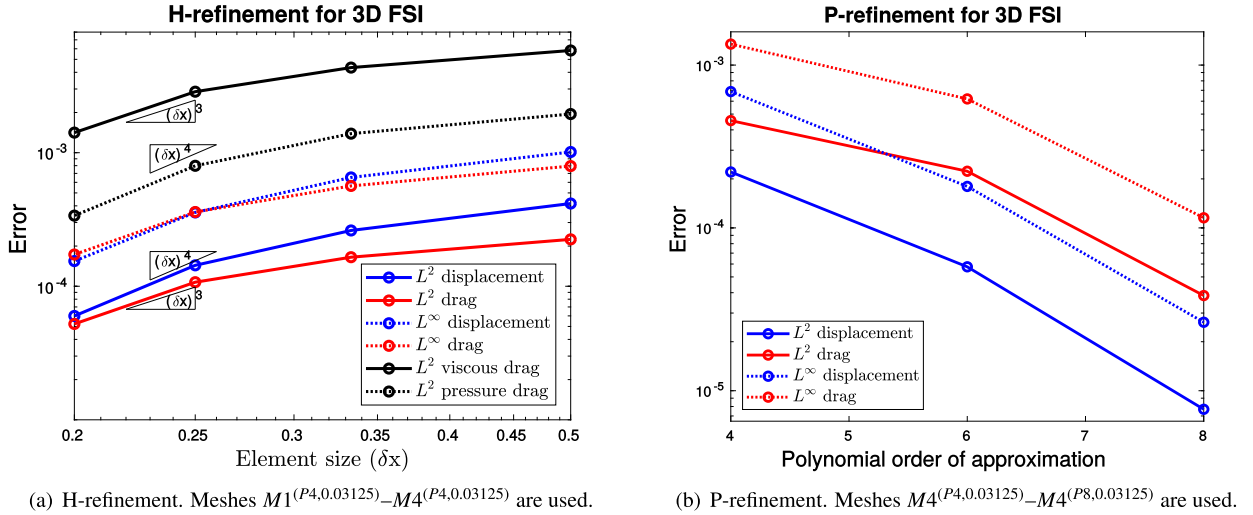
(a) H-refinement. Meshes $M1^{(P4,0.03125)}$–$M4^{(P4,0.03125)}$ are used.

(b) P-refinement. Meshes $M4^{(P4,0.03125)}$–$M4^{(P8,0.03125)}$ are used.

Fig. 19. Spatial convergence for the compliant wall channel 3D FSI benchmark.

$$F_p(t) = \int_{\Gamma_{fsi}(t)} (p\,\vec{n}_f) \cdot \vec{i}\, d\Gamma, \tag{78}$$

$$F_v(t) = -\int_{\Gamma_{fsi}(t)} [\mu(\nabla\mathbf{u} + (\nabla\mathbf{u})^T)\vec{n}_f] \cdot \vec{i}\, d\Gamma, \tag{79}$$

with

$$F_d(t) = F_p(t) + F_v(t). \tag{80}$$

We note that the number of elements in streamwise and spanwise directions is always even for all the meshes, so that no interpolation is required to obtain the midpoint displacement, since it is located at the intersection between the elements, where a GLL node always exists.

In this study, we investigate two error norms, L^2 and L^∞, defined as

$$L^2(q) = \sqrt{\frac{\int_0^{t_f} \left(q_{ref}(t) - q_{comp}(t)\right)^2 \, dt}{t_f}}, \tag{81}$$

$$L^\infty(q) = \max_{t \in [0, t_f]} \left| q_{ref}(t) - q_{comp}(t) \right|, \tag{82}$$

where q_{comp} is the quantity taken from the simulations at a particular refinement level, and q_{ref} is the corresponding reference value taken from a reference mesh solution, and the time $t_f = 25$ is set in the current simulations.

5.2. Results

5.2.1. H-refinement

The results of the h-refinement study with the meshes $M1 - M5$ using 4th-order polynomials and a time step size of $\delta t = 0.03125$ are shown in Fig. 19(a), where the $M5$ results with the same polynomial order and the time step are considered as a reference value, and the errors for the meshes $M1 - M4$ with respect to $M5$ mesh values are plotted. Fig. 19(a) shows that both L^2 and L^∞ errors of displacement exhibit expected 4th-order of convergence in the asymptotic limit. The order of convergence of the drag value is however reduced to the 3rd order, both for L^2 and L^∞ error norms. In order to investigate what hampers the convergence of the drag values, we look into the L^2 errors for the pressure and viscous drag separately, also plotted in Fig. 19(a). The results show that while the pressure drag shows the expected 4th-order of convergence, it is the viscous drag that converges with the 3rd order. The reason is that the viscous drag includes the first-order spatial derivatives of the velocity quantities in its definition. While velocities are approximated with the pth-order polynomials functions, their derivatives are consequently approximated by the $(p-1)$st order polynomials, which drops the rate of convergence of a quantity that depends on the spatial derivatives of the solution variables by an order of a derivative [60].

Table 4
Temporal convergence rates r obtained with the Richardson extrapolation for the midpoint displacement and the total flow drag on the compliant surface evaluated using the meshes $M2^{(P4,0.03125)} - M2^{(P4,0.125)}$.

Scheme	Midpoint displacement	Total flow drag
IE-ALE with GCL	0.9440	0.6387
CN-ALE	1.8272	1.5008

Table 5
Mesh, tolerance values, and a reference solution used for the solver tolerance study in the proposed compliant wall channel 3D FSI benchmark.

Mesh level	Polynomial order	Time step, δt	κ_s	κ_f	κ	Reference mesh
M2	P4	0.05	10^{-12}	$\left[10^{-6} : 10^{-2}\right]$	$\left[10^{-6} : 10^{-2}\right]$	$M2^{(P4,0.05)}$ with $\left(\kappa_s, \kappa_f, \kappa\right) = \left(10^{-12}, 10^{-6}, 10^{-6}\right)$

5.2.2. P-refinement

To study the FSI solver convergence with *p*-refinement, we choose the mesh $M4$ with 4th, 6th and 8th order polynomials and the same time step of $\delta t = 0.03125$, see Table 3, while the reference solution is provided by the mesh $M7$ with the 6th order polynomials and $\delta t = 0.03125$. The results of the *p*-refinement convergence study are shown in Fig. 19(b). The expected exponential order of convergence (linear in a semi-log plot) is observed for both displacement and drag. As expected, the slope of the convergence plot is steeper for the displacement versus drag errors, commensurate with the fact that displacements are approximated with higher-order polynomial functions as discussed above.

5.2.3. Temporal refinement

For a temporal convergence verification, the mesh $M2$ with 4th-order polynomials is used, with the time steps $\delta t = 0.125$, $\delta t = 0.0625$ and $\delta t = 0.03125$, with a reference solution taken from $M2^{(P4, 0.01)}$, as specified in Table 3. In the temporal convergence study, the two schemes which showed a second-order convergence in the fluid-only tests, namely, the IE-ALE with GCL, and CN-ALE (see Sec. 2.2.2) are compared. The results are shown in Fig. 20. It is interesting to see that, although IE-ALE with GCL showed a second-order temporal convergence in fluid-only tests on deforming meshes, its accuracy drops to the first order in the fully coupled FSI problem, while the CN-ALE scheme preserves the second order accuracy in the fully coupled problem. For a better estimation of the convergence slope, we perform a Richardson extrapolation of errors with the three chosen time steps, and calculate the convergence rate r as

$$r(q) = \frac{1}{\ln(2)} \ln \left(\frac{\left| q(M2^{(P4,0.125)}) - q(M2^{(P4,0.0625)}) \right|}{\left| q(M2^{(P4,0.0625)}) - q(M2^{(P4,0.03125)}) \right|} \right), \tag{83}$$

where q is the quantity to be estimated, evaluated with the different meshes. In the current study, q is taken to be the time-averaged value of the midpoint displacement and the total flow drag on the compliant surface. The results of Richardson extrapolation are shown in Table 4. Table 4 confirms the conclusion that CN-ALE scheme preserves the second-order of accuracy, while IE-ALE scheme does not. This shows that, in order to keep a nominal order of convergence in the fully coupled problem, not only do both component codes have to have a time stepping scheme of the required nominal order of accuracy, but the interface coupling scheme of the same order of accuracy is also required. This also shows the importance of verification studies and convergence tests on the fully coupled FSI problem. We also note a slightly lower rate of a temporal convergence of drag in both schemes compared to a displacement, which can also be seen in Fig. 20. The reason for this reduction might be associated with the fact that the drag is related to the velocity variables rather than displacements, and the nominal order of accuracy of the Newmark scheme is lower for velocities than for displacements.

Temporal dynamics. To evaluate the effect of spatial and temporal refinement on the dynamics of the quantities of interest, we plot the temporal series of the vertical midpoint wall displacement and the total flow drag on the compliant surface in Fig. 17 for the different meshes. For the displacement evolution, Fig. 17(a) demonstrates that all the cases with different levels of *h*-refinement, *p*-refinement and time step, show essentially identical values. The drag evolution shown in Fig. 17(b) is, however, more sensitive to a spatial refinement, showing that it requires finer meshes and/or higher polynomial orders to converge the values of drag. From Fig. 17(c), Fig. 17(d), it cal also be seen that the meshes with one and two layers of solid elements produce identical results, testifying that the two layers of solid elements provide an adequate resolution for the solid. Since displacement is less sensitive to a spatial refinement compared to a drag, this means that in the situations where primarily a displacement of the structure is of interest, the mesh size (the total number of degrees of freedom) could be reduced to save cost.

This high sensitivity of drag to a spatial resolution can explain why it is difficult to obtain ideal convergence slopes with *h*- and *p*-refinements across a large range of h, p levels in the FSI problem, i.e., for meshes that differ significantly in their spatial resolutions, as observed in Fig. 19. Since the drag force is the one that drives the motion of the solid, which in turns drives the fluid, the spatial resolution of drag now also effects the temporal dynamics, and not only the spatial
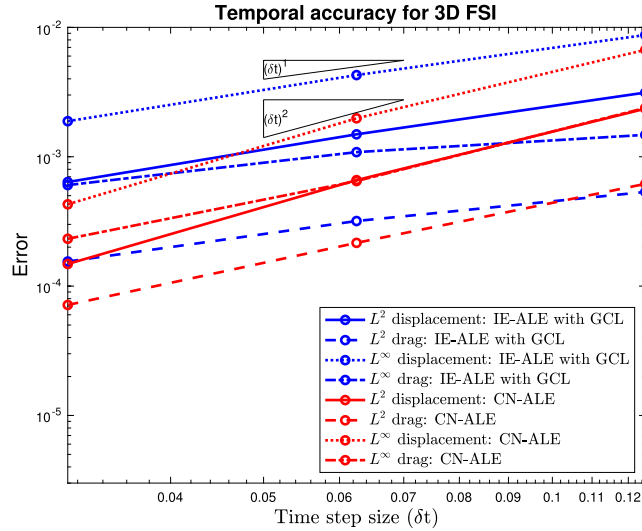
Fig. 20. Temporal convergence for the compliant wall channel 3D FSI benchmark. Meshes $M2^{(P4,0.03125)}$–$M2^{(P4,0.125)}$ are used.
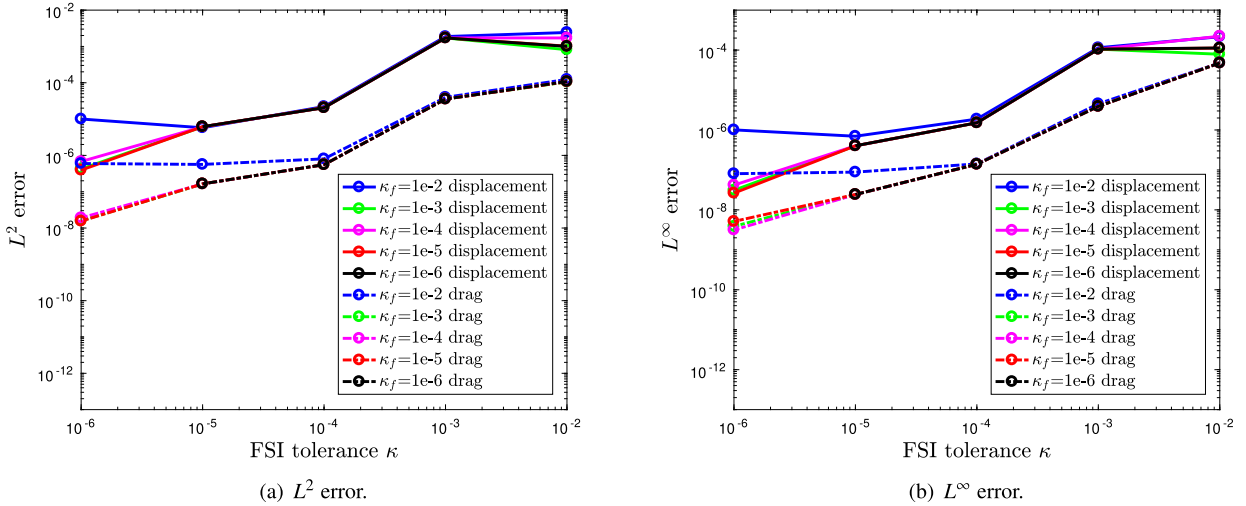

Fig. 21. Effect of tolerances on the solution errors for compliant wall channel 3D FSI benchmark.

accuracy. A slightly different temporal dynamics at different spatial resolutions results in a fact that the values that are being compared are now also shifted in time. For the error estimates such as these obtained with Eq. (81), Eq. (82), when the errors are compared at the same time step, the outcome is that the temporal differences introduced by different spatial resolutions now implicitly enter the spatial convergence results, which makes it difficult to separate temporal and spatial errors, and obtain an anticipated spatial convergence rate across a wide range of resolutions. It would be interesting to devise improved error metrics, for example, using a temporal convolution of the values at different spatial resolutions, to assess the applicability of such enhanced error measures to the coupled multi-physics problems, which will be investigated in the future work.

5.2.4. Tolerance study

We now turn our attention to the effect of the FSI convergence criteria κ and the fluid solver tolerance κ_f on the L^2 and L^∞ errors of the quantities of interest in the FSI problem. It is important to quantify this effect, since higher tolerances can be associated with faster solver execution times but can incur larger global errors. Understanding the tradeoff is helpful for practical applications. In the current study, the mesh $M2^{(P4,0.05)}$ is used with various values of the FSI and fluid solver tolerances κ, κ_f ranging from 10^{-2} to 10^{-6} as given in Table 5. Solid solver tolerance is fixed at 10^{-12} in all the studies. The reason we do not vary the solid tolerance is because the solid iterations account for a small fraction of the total computational time of the coupled FSI solver, due to a dominance of the computational cost by the pressure Poisson solution of the Navier-Stokes equations, and due to a relatively small size of a solid domain compared to a fluid domain. Keeping a
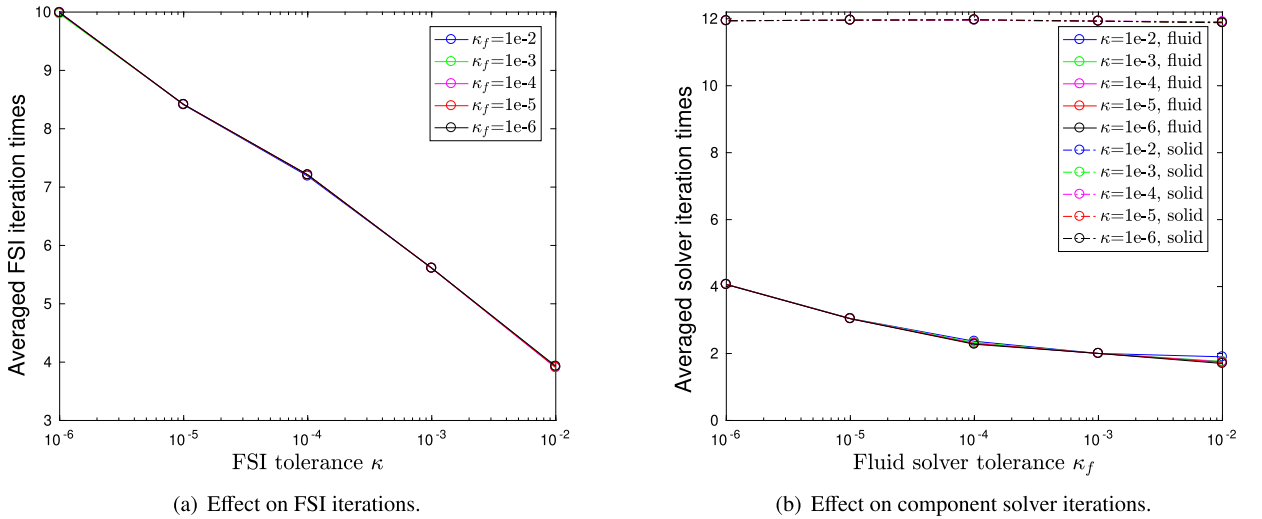
(a) Effect on FSI iterations.

(b) Effect on component solver iterations.

Fig. 22. Effect of tolerances on the number of solver iterations for compliant wall channel 3D FSI benchmark.

solid solver tolerance at a very low level as in the current tests ensures that the errors from the iterative convergence of the solid solver are minimized, at essentially no additional cost.

The L^2 and L_∞ errors for the vertical wall displacement and the total flow drag on a compliant surface at various fluid and FSI tolerances are shown in Fig. 21 (note that there is no data point for the $(\kappa_s, \kappa_f, \kappa) = (10^{-12}, 10^{-6}, 10^{-6})$ case, which corresponds to the reference mesh, and for which the error is identically zero). One can see that for both displacement and the drag, the effect of the fluid solver tolerance κ_f is negligible as long as the tolerance does not exceed the value of $\kappa_f = 10^{-3}$, which means that this value of the fluid tolerance should in general be sufficient for convergence. The strong effect of the FSI tolerance κ is pronounced for both quantities, with errors decreasing by three to four orders of magnitude when κ is reduced from 10^{-2} to 10^{-6}. However, for the lowest fluid solver tolerance $\kappa_f = 10^{-2}$, the effect of tightening the FSI solver tolerance κ is of diminishing return, since the error is then dominated by a poor fluid solver convergence and is not improved by a stronger fluid-solid coupling.

To assess the increase in the computational cost associated with the tightening of the convergence criteria, the number of iterations taken by the component solvers and by the FSI interface coupling routine in response to different values of the convergence tolerances is shown in Fig. 22. The number of iterations taken by the solvers at each time step is averaged over the entire time of the simulations, thus an averaged number of iterations is presented. We see that, as expected, the number of FSI iterations do not depend on the fluid solver tolerance κ_f, while increasing the FSI tolerance κ from 10^{-6} to 10^{-2} reduces the average number of iterations from ten to four, thus reducing the global solver cost by approximately 2.5 times. Fig. 22(b) shows that the number of solid solver iterations depends neither on the fluid tolerance nor the FSI tolerance, as expected. The number of fluid solver iterations does not depend on the FSI tolerance either, however, it does depend on the fluid tolerance. While Fig. 21 showed that the fluid tolerance can be increased from 10^{-6} to 10^{-3} without affecting the accuracy, Fig. 22(b) shows that this increase will decrease the number of iterations from four to two which will, essentially, cut the total computational cost by two, since the cost of the fluid solver, due to a Poisson equation solution, far exceeds that of the solid solver. Therefore, for practical FSI implementations where a cost versus accuracy tradeoff may be considered, we recommend increasing the fluid solver tolerance while keeping the FSI tolerance as low as possible.

6. Fluid-structure interaction in a 3D turbulent channel with a compliant wall

6.1. Problem formulation

In this section, we extend the developed FSI solver to a Direct Numerical Simulation of an interaction of a turbulent flow with a nonlinearly elastic compliant wall. Previous computational studies of the interaction between the turbulent flow and an elastic surface were primarily confined to a zero-thickness spring-backed membrane model for the solid material [40,61,62]. In addition to being a very simplistic model that neglects many important effects pertinent to structural dynamics related to multi-dimensionality and non-linearity, the spring-backed membrane model does not allow for longitudinal wall motions, which have been found to be important [63], especially during the interaction with turbulence, where the properties of the fluctuating field are crucial in determining the global structure of turbulence, and their artificial suppression might draw an incomplete picture. In a recent computational study, Rosti and Brandt [41] used a monolithic FSI approach combined with a 2nd-order finite difference scheme to model the interaction of an incompressible flow in a channel with a hyperelastic Mooney-Rivlin material wall. With a monolithic approach, an FSI interface is not resolved, but

Table 6
Number of elements and the polynomial order of approximation for the two meshes used in a turbulent channel flow case.

Mesh	Fluid/Solid	Number of Elements, (n_x, n_y, n_z)	Polynomial order, N
$M1$	Fluid	$(50, 10, 10)$	7
	Solid	$(50, 2, 10)$	7
$M2$	Fluid	$(60, 10, 12)$	7
	Solid	$(60, 2, 12)$	7

Table 7
Mesh resolution in wall units in undeformed configuration for the two fluid meshes used in the turbulent channel flow case based on u_τ of the corresponding rigid wall case. Wall units are defined as $L^+ = L u_\tau / \nu$, with $u_\tau = \sqrt{\tau_w/\rho}$ being wall friction velocity, τ_w is wall shear stress, $Re_\tau = u_\tau H/\nu$. ΔL^+, min corresponds to a minimum distance between the grid points across all elements and GLL points, while ΔL^+, max corresponds to a maximum distance. Difference in uniform x and z directions is solely due to a non-uniform GLL points distribution.

Mesh	Re_τ	ΔX^+, min	ΔX^+, max	ΔY^+, min	ΔY^+, max	ΔZ^+, min	ΔZ^+, max
$M1$ Fluid	179.9946	2.9015	9.4695	0.6245	18.0867	7.2538	23.6711
$M2$ Fluid	177.8704	2.3906	7.7978	0.6171	17.8731	5.9729	19.4928

implicitly embedded into the computational cells analogously to the methodology of immersed boundary techniques [64]. This leads to a low-order representation of the interface and the surrounding near-wall velocities, which can create some numerical deficiencies in a case of a turbulent flow.

The presented simulation is the first attempt to apply a high-order interface-resolving FSI solver to a Direct Numerical Simulation of a turbulent channel flow interacting with a nonlinear, hyperelastic wall. The setup of the problem is similar to the one described in the previous section. A fluid flow in an originally rectilinear box of the length $(L_x, L_y, L_z) = (4\pi H, 2H, 2\pi H)$ interacts with a nonlinearly elastic solid layer of the thickness $D = 0.2H$ at its top boundary. The boundary conditions for the fluid are: 1) periodic in streamwise and spanwise directions, 2) a no-slip wall enforced at the bottom boundary $Y = -H$, 3) fluid-structure interface at the top wall $Y = H$. A forcing function is applied in a streamwise direction to keep the mass flow rate constant [57]. The Reynolds number of the flow based on the bulk mean velocity U and a channel half-width H is set as $Re = UH/\nu = 2800$, which for channel flow is in the turbulent regime [65]. An illustration of the domain geometry for the fluid and the solid layers and the overall problem setup is presented in Fig. 23.

A fully-developed turbulent channel flow with rigid walls is first obtained before the interaction with a compliant solid is initiated. To trigger the transition to turbulence in a channel, the following initial conditions for the fluid flow are specified [66]

$$
\begin{aligned}
u_x/U &= 5(1 - (\tilde{y})^4)/4 + 0.3 \cos(12\tilde{z}) e^{0.5 - 32.4(1 - |\tilde{y}|)^2}(1 - |\tilde{y}|), \\
u_y/U &= 0, \\
u_z/U &= 21.6 \sin(12\tilde{x}) e^{-32.4(1 - |\tilde{y}|)^2}(1 - |\tilde{y}|),
\end{aligned}
\tag{84}
$$

where $\{\tilde{x}, \tilde{y}, \tilde{z}\} = \{x/H, y/H, z/H\}$. Initial perturbations are necessary in this case, since discretization errors in a spectral-element method are intrinsically low and, by themselves, are unable to trigger transition to turbulence. Additionally, the channel flow with the current relatively low Reynolds number is linearly stable. The specified initial conditions correspond to an initial perturbation in a form of elongated high- and low-speed streaks with superimposed spanwise velocity perturbations. According to a recent research, this type of perturbations triggers auto-generating mechanisms of turbulence, via which the turbulence is initiated and sustained [67–69].

The simulations are run on two meshes. The number of fluid elements for the first mesh is $(n_{f,x}, n_{f,y}, n_{f,z}) = (50, 10, 10)$, and for the second mesh it is $(n_{f,x}, n_{f,y}, n_{f,z}) = (60, 10, 12)$, while the polynomial order of $N = 7$ is used for both meshes for a spectral element discretization in space, see Table 6. The element spacing in the y direction is given in [66], while the element sizes in x and z directions are uniform. Note that [66] used the same spectral-element code Nek5000 in their study of a turbulent rigid-wall channel flow with $Re = 2800$. After running the decoupled fluid solver for $200H/U$ time units, turbulence becomes statistically stationary [66]. Turbulent statistics are subsequently gathered over $50H/U$ time units. Before moving on to the FSI study, turbulent statistics were validated against the results of Sprague et al. [66] and Kim et al. [65], and a good agreement was obtained for both meshes (not shown here). Based on the calculated wall shear stress, the obtained grid resolution in wall units is documented in Table 7 for the two meshes.

After a simulation time of $250H/U$ time units, the fluid-structure interaction is initiated. An elastic solid layer added on top of the fluid domain covers the whole extent of the top channel boundary and has the dimensions of $(L_x, L_y, L_z) = (4\pi H, 0.2H, 2\pi H)$. A solid layer is modeled by a nonlinear hyperelastic St. Venant-Kirchoff material model as described in Sec. 2.1.1. The boundary conditions for the solid are: 1) periodic in streamwise and spanwise directions, 2) fluid-structure interface at the lower solid boundary $Y = H$, 3) clamped wall at the top solid boundary $Y = 1.2H$. The solid boundary locations are given in an undeformed configuration. The number of elements for the solid are: $(n_{s,x}, n_{s,y}, n_{s,z}) = (50, 2, 10)$
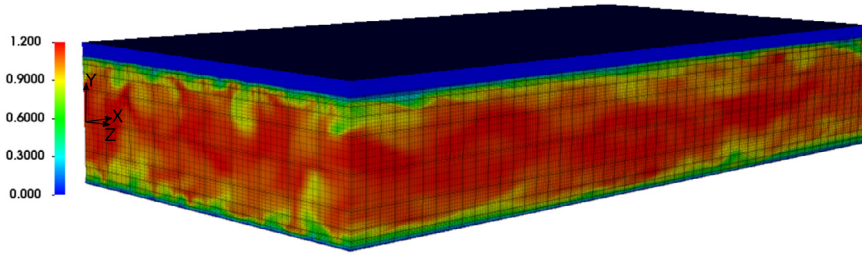
Fig. 23. FSI in a turbulent channel domain geometry and problem setup, including the computational grid for the fluid with GLL points. The blue layer on top corresponds to a hyperelastic solid coating. The snapshot of the streamwise fluid velocity (refer to the colorbar for values) shows a streamwise-spanwise view of high- and low-speed streaks in a turbulent channel flow. Results with the mesh $M1$ are shown.
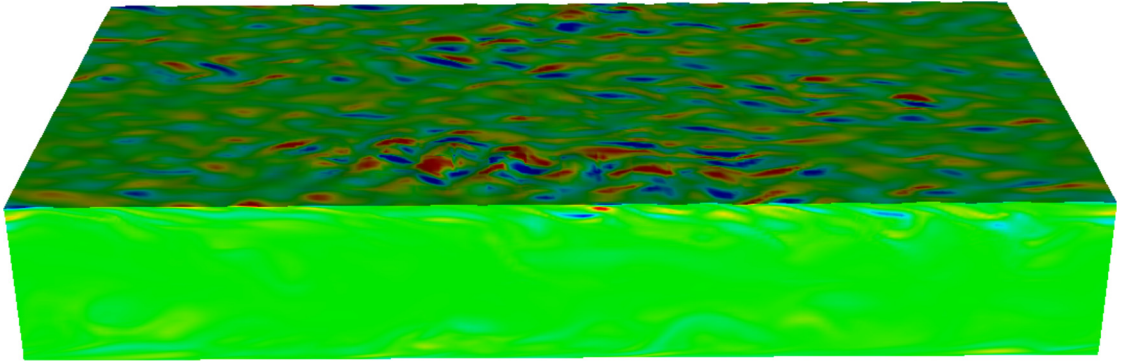
Fig. 24. Instantaneous streamwise vorticity and the deformation of the fluid-solid interface with mesh $M1$ at a time $26H/U$, color bar from -10 (blue) to 10 (red).

for the first mesh, $(n_{s,x}, n_{s,y}, n_{s,z}) = (60, 2, 12)$ for the second mesh, with the polynomial order of $N = 7$ for both meshes, as documented in Table 6. The element sizes are uniform in all three directions. The material properties for the solid are set as density $\rho_s = 10\,\rho_f$, Young's modulus as $E = 5\,\rho_f U^2$, and Poisson's ratio as $\nu_s = 0.3$. These material properties can be converted into λ_s and μ_s as Lamé constants in a constitutive relation, Eq. (9). A measure of the wall inertia relative to the fluid is often presented as the non-dimensional parameter $C_m = (\rho_s D)/(\rho_f H)$. The higher C_m is, the heavier is the wall and the fewer interactions are expected between the solid and the fluid, while for a lower C_m the situation is the opposite. In the current simulations, the value of $C_m = 2$ is used, which corresponds to a moderately light wall considered in previous theoretical studies [70] and in simulations [40]. Another material parameter that characterizes a potential of the structure to stimulate strong coupling processes with the fluid is the shear wave speed. Previous studies have shown that a strong interaction can be expected if the elastic shear wave speed is less than the flow speed [39,71]. Shear wave speed for the current solid is $c_t = \sqrt{E/(2(1+\nu)\rho_s)} = 0.438\,U$, which corresponds to a soft wall capable of interactions with the fluid. The initial conditions for the solid are at zero displacements, velocities and acceleration. The FSI simulations are advanced with the time step $\delta t = 0.005\,H/U$, which leads to a Courant number of approximately 0.4. Three FSI iterations were found sufficient for stability.

6.2. Results

Although the solid material surface in contact with the fluid is originally flat, a fluid-solid interface soon develops small-scale deformations from the influence of the fluctuating pressure and viscous forces in a turbulent flow. Fig. 24 shows a visualization of the instantaneous streamwise vorticity and a top surface deformation at a time $26H/U$ from the beginning of the FSI simulations, where the small-scale wrinkles originating in the top surface deformation field can be observed. The unsteady interaction processes between the fluid flow and a hyperelastic compliant wall significantly change the structure of turbulence as can be seen from Fig. 25(a) and Fig. 25(b), where streamwise vorticity slices at $Y^+ = 5$ from the lower and upper walls are presented to show the difference between the bottom rigid and the top flexible surfaces in the current simulations at a time of $26H/U$. Note that the location of the slices for visualization refers to an undeformed configuration. It can be seen that elongated quasi-streamwise vortices typical of a classical near-wall turbulence in a presence of a rigid wall [72] (see Fig. 25(a)) are broken down by a flexible wall in Fig. 25(b), and a significant amount of small-scale vorticity is generated, forming structures that are no longer primarily aligned with the mean flow direction.

We next present the time series of the total flow drag defined in Eq. (77) for both the bottom and top walls for the FSI and no-FSI turbulent channel flow cases in Fig. 26 for the two meshes. Without FSI, the flow drag among the lower and upper walls exhibits similar, relatively smooth time dynamics. We also note low-frequency fluctuations associated with
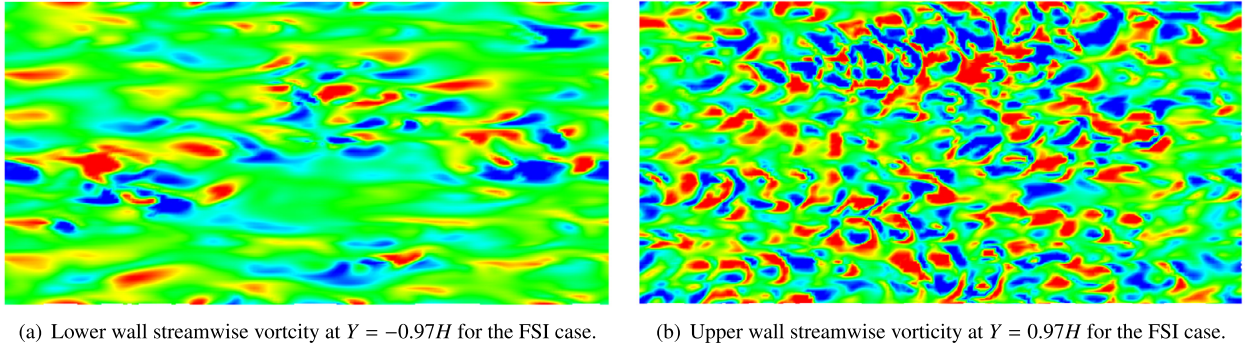
(a) Lower wall streamwise vortcity at $Y = -0.97H$ for the FSI case.

(b) Upper wall streamwise vorticity at $Y = 0.97H$ for the FSI case.

Fig. 25. Instantaneous snapshots of streamwise vorticity at $Y^+ = 5$ from the lower and upper surfaces in a turbulent channel flow with mesh $M1$ at a time $26H/U$, color bar from -2 (blue) to 2 (red). Note the change in the color bar compared to Fig. 24. The location of the planes for visualization refers to an undeformed configuration.
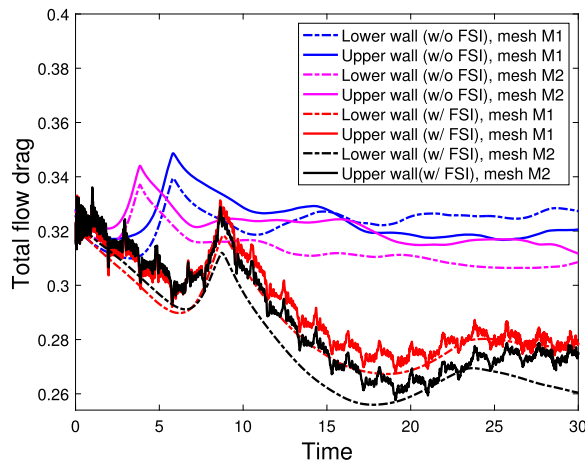

Fig. 26. Comparison of the total flow drag for the lower and upper walls with and without FSI in a turbulent channel flow with the two meshes. Time is normalized with H/U.

the dynamics of the near-wall turbulent coherent structures, which, in low-Reynolds number flows as simulated here, are relatively large in size relative to the channel dimensions and exert a noticeable long-lasting influence on the surface drag [73,74], which can also explain the difference in the lower and upper surface drag curves, exposed to their own local near-wall structures. The drag on the upper wall shows completely different dynamics when FSI is introduced. Low-frequency motions still persist, but, for the upper elastic wall, these motions are further superimposed by high-frequency fluctuations due to a small-scale turbulence, potentially caused by surface wrinkles, as can be seen in Figs. 24, 25. The two meshes show a conceptually similar dynamics of the drag force at the rigid and elastic walls in an FSI flow. The quantitative difference between the drag values obtained with the two meshes can be attributed to the same mechanisms that cause the time series of drag on the lower and upper walls to differ in the rigid-wall channel, i.e., the low-frequency dynamics of coherent structures, which is sensitive to any perturbation, including the difference in mesh. Variability in local behavior due to coherent structure dynamics is not expected to influence the flow statistics. However, long simulation times are required for collecting reliable turbulent flow statistics, which might be longer in the presence of fluid-structure interaction compared to a rigid-wall case. Further studies of the turbulent fluid-structure interaction case, including investigation of the turbulent flow statistics and structure in the presence of a flexible wall, as well as the influence of the grid resolution on the statistics in the turbulent FSI case, will be presented in the future papers.

7. Conclusions

This paper presents a high-order in space and second-order in time computational methodology for a solution of a strongly-coupled fluid-structure interaction problem. The methodology is based on a spectral-element formulation of both the solid and the fluid equations. Solid equations adapt a geometrically nonlinear framework using a St. Venant-Kirchoff material model, while fluid equations solve an incompressible Navier-Stokes equations system on deforming meshes based on Arbitrary Eulerian Lagrangian formulation. The coupling is accomplished via a fixed point iteration approach with Aitken relaxation, which is known to be a robust methodology that allows to achieve stable results in the presence of an added

mass effect [75,76]. In addition to a development of a high-order solver itself, we have also proposed a comprehensive verification methodology to demonstrate a high-order spatial and a second-order temporal accuracy of the approach in a consistent manner, which consists of *h*-, *p*- and temporal refinement tests for both the component solvers, and the coupled fluid-structure interaction problem formulation. Additionally, we have demonstrated a good performance of the methodology on commonly accepted fluid-structure interaction benchmarks, including a flow-induced vibration of a two-dimensional cantilever beam attached to a circular cylinder [33], and a pressure-driven flow in a three-dimensional pipe with flexible walls [38].

A polynomial spectral accuracy of the approach with the corresponding *h*- and *p*-refinement tests, and the expected second-order temporal convergence of the method, was first demonstrated on an elastostatics and elastodynamics solid formulation using a method of manufactured solutions, and subsequently on a solution of the incompressible fluid flow equations against an analytical solution of convecting Walsh's eddies [58]. For the fluid solver, following a preliminary conclusion achieved by Formaggia and Nobile [46] on a model problem of a linear advection-diffusion equation, it was demonstrated on an example of the full Navier-Stokes equation system that the 2nd-order BDF scheme in a conservative formulation with a linear in time geometry update (IE-ALE scheme) achieves only a 1st order temporal accuracy on deforming meshes unless the Geometric Conservation Law (GCL) is satisfied. It was also shown that the expected 2nd-order accuracy is recovered if the GCL is implemented. It was also demonstrated for the first time that when the IE-ALE scheme with GCL is applied to a fully coupled FSI problem, where both the fluid and the solid equations are discretized with the second-order schemes (BDF2 for fluid and Newmark for solid), the order of accuracy of the coupled problem reduces to one. To alleviate this problem, a new ALE solver was developed that uses a Crank-Nicholson type geometry update, matching the solid interface update from the Newmark code. Note that GCL is not needed with the CN-type update, because in this case the ALE geometry is updated with the 2nd-order accuracy. A global 2nd-order accuracy of the approach was verified on a fully coupled FSI problem using self-convergence tests. The developed implementation ensures a perfect match of both the interface velocities and displacements between the fluid and the solid solver, thus ensuring a stable and consistent formulation in the considered case of large displacements allowed by a geometrically nonlinear solid formulation.

To allow for a consistent testing of a high-order method on a fully coupled FSI problem, a new computational benchmark has been developed, which consists of a fluid flow in a three-dimensional channel bounded by one rigid and one flexible wall. High-order convergence of spectral element methods can only be achieved for smooth solutions. Special care has thus been taken to develop a benchmark which ensures smoothness of a fully coupled FSI solution in a time-dependent formulation. This involved specification of initial and boundary conditions that are consistent throughout the coupled fluid and solid domains, and are smooth in space and time. The new proposed framework allowed us to demonstrate, for the first time, a possibility of obtaining a high-order spatial convergence with *h*- and *p*-refinement on a fully coupled FSI problem, and also confirmed an expected second-order temporal convergence of the CN-ALE scheme. The convergence study of the fully coupled problem also exemplified a potential need to revisit the definition of the error norms currently employed in single-physics problems, systematically assess their applicability to multi-physics problems, and, perhaps, devise improved error metrics for the FSI problems, to be explored in the future work.

The benchmark was also utilized to assess the influence of the iterative solvers' tolerances on the global error, which was not highlighted before. A conclusion from this study was that the fluid solver tolerance does not significantly affect the results and can be safely set to a relatively high number resulting in only two fluid solver iterations. However, a tolerance of the FSI solver can have a significant impact on the results, generally reducing the global error by an order of magnitude if the tolerance is reduced by an order of magnitude. Developing strongly-coupled FSI approaches that do no rely on fixed-point iterations, including generalized Robin boundary conditions, such as some recent attempts published in [28–32], is therefore a promising avenue to proceed and is worth of an investment, which will be considered in our future work. The developed high-order FSI methodology was ultimately applied to a Direct Numerical Simulation of a turbulent flow in a channel interacting with a hyperelastic compliant wall. This is the first attempt of applying an interface-resolving FSI methodology to a fluid-structure interaction problem involving a turbulent flow and a finite-thickness elastic wall. An ability to predict near-wall turbulent fluctuations with high-order accuracy in the presence of a flexible wall opens up further avenues for research: for example, in the design of passive compliant surfaces capable of controlling near-wall turbulence, which may reduce drag or enhance turbulent mixing and heat transfer, for a variety of engineering applications.

CRediT authorship contribution statement

YiQin Xu: Numerical methodology development, Post-processing and data analysis, Writing – original draft preparation. **Yulia Peet:** Supervision, Funding acquisition, Writing – reviewing and editing.

Declaration of competing interest

The authors declare that they have no known competing financial interests or personal relationships that could have appeared to influence the work reported in this paper.

Acknowledgements

This work has been supported by NSF CBET-1707075, NSF CMMI-1762827, and NSF CAREER-1944568 grants. The computational time was provided by NSF XSEDE research allocation on TACC Stampede2 system.

References

[1] K.Y. Billah, R.H. Scanlan, Resonance, Tacoma Narrows bridge failure, and undergraduate physics textbook, Am. J. Phys. 59 (1991) 118–124.
[2] E. Livne, Aircraft active flutter suppression: State of the art and technology maturation needs, J. Aircr. 55 (2018) 410–450.
[3] J.S. Rao, Turbomachine Blade Vibration, New Age International Publishers, 2005.
[4] D.H. Jones, A.Y. Nehru, J. Skinner, The impact fretting wear of a nuclear reactor component, Wear 106 (1985) 139–162.
[5] P.W. Carpenter, A.D. Garrad, The hydrodynamic stability of flow over Kramer-type compliant surfaces, Part 1: Tollmien-Schlichting instabilities, J. Fluid Mech. 155 (1985) 465–5120.
[6] A.E. Dixon, A.D. Lucey, P.W. Carpenter, The optimization of viscoelastic coating walls for transition delay, AIAA J. 32 (1994) 256–267.
[7] M. Gad-el-Hak, Compliant coatings for drag reduction, Prog. Aerosp. Sci. 38 (2002) 77–99.
[8] T.B. Benjamin, Fluid flow with flexible boundaries, in: Henry Görtler (Ed.), Proceedings of the 1st International Congress on Applied Mechanics, Munich, Germany, 1964, Springer Verlag Berlin Heidelberg GmbH, 1966.
[9] M.O. Deville, P.F. Fischer, E.H. Mund, High-Order Methods for Incompressible Fluid FLow, Cambridge University Press, 2002.
[10] B. Cockburn, G.E. Karniadakis, C.-W. Shu, Discontinuous Galerkin Methods: Theory, Computation and Applications, Lecture Notes in Computational Science and Engineering, vol. 11, Springer, 1991.
[11] Z.J. Wang, K. Fidkowski, R. Abgrall, F. Bassi, D. Caraeni, A. Cary, H. Deconinck, R. Hartmann, K. Hillewaert, H. Huynh, N. Kroll, G. May, P.-O. Persson, B. van Leer, M. Visbal, High-order CFD methods: current status and perspective, Int. J. Numer. Methods Fluids (2012) 1–42, https://doi.org/10.1002/fld.
[12] G. Pena, C. Prud'homme, Construction of a high-order fluid-structure interaction solver, J. Comput. Appl. Math. 234 (2010) 2358–2865.
[13] H. Baek, G.E. Karniadakis, A convergence study of a new partitioned fluid-structure interaction algorithm based on fictitious mass and damping, J. Comput. Phys. 231 (2012) 629–652.
[14] B. Froehle, P.-O. Persson, A high-order discontinuous Galerkin method for fluid-structure interaction with efficient implicit-explicit time stepping, J. Comput. Phys. 272 (2014) 455–470.
[15] J.P. Sheldon, S.T. Miller, J.S. Pitt, A hybridizable discontinuous Galerkin method for modeling fluid-structure interaction, J. Comput. Phys. 326 (2016) 91–114.
[16] A. Verkaik, M. Hulsen, A. Bogaerds, F. van de Vosse, An overlapping domain technique coupling spectral and finite elements for fluid-structure interaction, Comput. Fluids 123 (2015) 235–245.
[17] Y. Bazilevs, K. Takizawa, T.E. Tezduyar, Computational Fluid-Structure Interaction Methods and Applications, A John Wiley & Sons, Ltd, 2013.
[18] Y. Yu, H. Baek, M.L. Bittencourt, G.E. Karniadakis, Mixed spectral/hp element formulation for nonlinear elasticity, Comput. Methods Appl. Mech. Eng. 213–216 (2012) 42–57.
[19] S. Dong, Z. Yosibash, A parallel spectral element method for dynamic three-dimensional nonlinear elasticity problems, Comput. Struct. 87 (2009) 59–72.
[20] H. Baek, G.E. Karniadakis, Sub-iteration leads to accuracy and stability enhancements of semi-implicit schemes for the Navier-Stokes equations, J. Comput. Phys. 230 (2011) 4384–4402.
[21] G. Pena, C. Prud'homme, A. Quarteroni, High order methods for the approximation of the incompressible Navier-Stokes equations in a moving domain, Comput. Methods Appl. Mech. Eng. 209–212 (2012) 197–211.
[22] P.-O. Persson, J. Bonet, J. Peraire, Discontinuous Galerkin solution of the Navier-Stokes equations on deformable domains, Comput. Methods Appl. Mech. Eng. 198 (2009) 1585–1595.
[23] A. Patera, A spectral element method for fluid dynamics: laminar flow in a channel expansion, J. Comput. Phys. 54 (1984) 468–488.
[24] N.-H. Kim, Introduction to Nonlinear Finite Element Analysis, Springer US, 2015.
[25] G.A. Holzapfel, Nonlinear Solid Mechanics: A Continuum Approach for Engineering, 1st edition, Wiley, 2000.
[26] U. Küttler, W.A. Wall, Fixed-point fluid-structure interaction solvers with dynamic relaxation, Comput. Mech. 43 (2008) 61–72.
[27] A. Aitken, On Bernoulli's numerical solution of algebraic equations, Proc. R. Soc. Edinb. 46 (1926) 289–305.
[28] S. Deparis, M.A. Fernández, L. Formaggia, Acceleration of a fixed point algorithm for fluid-structure interaction using transpiration conditions, ESAIM: M2AN 37 (2003) 601–616.
[29] S. Badia, F. Nobile, C. Vergara, Fluid-structure partitioned procedures based on Robin transmission conditions, J. Comput. Phys. 227 (2008) 7027–7051.
[30] J. Degroote, K.-J. Bathe, J. Vierendeels, Performance of a new partitioned procedure versus a monolithic procedure in fluid-structure interaction, Comput. Struct. 87 (2009) 793–801.
[31] Y. Yu, H. Baek, G.E. Karniadakis, Generalized fictitious methods for fluid-structure interactions: Analysis and simulations, J. Comput. Phys. 245 (2013) 317–346.
[32] J.W. Banks, W.D. Henshaw, D.W. Schwendeman, An analysis of a new stable partitioned algorithm for FSI problems. Part I: incompressible flow and elastic solids, J. Comput. Phys. 269 (2014) 108–137.
[33] S. Turek, J. Hron, Proposal for numerical benchmarking of fluid-structure interaction between an elastic object and laminar incompressible flow, in: H.-J. Bungartz, M. Schäfer (Eds.), Fluid-Structure Interaction, vol. 53, Springer, Berlin, Heidelberg, 2006, pp. 371–385.
[34] W.A. Wall, E. Ramm, Fluid–structure interaction based upon a stabilized (ALE) finite element method, in: S. Idelsohn, E. Oñate, E. Dvorkin (Eds.), Computational Mechanics – New Trends and Applications (Proceedings of WCCM IV), CIMNE, Barcelona, 1998.
[35] Z. Dou, A. Rips, N. Welsh, J.-H. Seo, R. Mittal, Flow-induced flutter of hanging banners: experiments and validated computational models, in: 2018 Fluid Dynamics Conference, 2018.
[36] L. Formaggia, J.-F. Gerbeau, F. Nobile, A. Quarteroni, On the coupling of 3D and 1D Navier-Stokes equations for flow problems in compliant vessels, Comput. Methods Appl. Mech. Eng. 191 (2001) 561–582.
[37] K.-J. Bathe, G.A. Ledezma, Benchmark problems for incompressible fluid flows with structural interactions, Comput. Struct. 85 (2007) 628–644.
[38] M.A. Fernández, J. Mullaert, M. Vidrascu, Generalized Robin-Neumann explicit coupling schemes for incompressible fluid-structure interaction: Stability analysis and numerics, Int. J. Numer. Methods Eng. 101 (2015) 119–229.
[39] M. Gad-el-Hak, R.F. Blackwelder, J.R. Riley, On the interaction of compliant coatings with boundary-layer flows, J. Fluid Mech. 140 (1984) 257–280.
[40] E. Kim, H. Choi, Space-time characteristics of a compliant wall in a turbulent channel flow, J. Fluid Mech. 756 (2014) 30–53.
[41] M.E. Rosti, L. Brandt, Numerical simulation of turbulent channel flow over a viscous hyper-elastic wall, J. Fluid Mech. 830 (2017) 708–735.
[42] G. Hou, J. Wang, A. Layton, Numerical methods for fluid-structure interaction – A review, Commun. Comput. Phys. 12 (2012) 337–377.
[43] Y.T. Peet, P.F. Fischer, Legendre spectral element method with nearly incompressible materials, Eur. J. Mech. A, Solids 44 (2014) 91–103.
[44] K.-J. Bathe, Finite Element Procedures, 1 ed., Prentice-Hall, 1996.

[45] B.E. Merrill, Y.T. Peet, Moving overlapping grid methodology of spectral accuracy for incompressible flow solutions around rigid bodies in motion, J. Comput. Phys. 390 (2019) 121–151.

[46] L. Formaggia, F. Nobile, Stability analysis of second-order time accurate schemes for ALE-FEM, Comput. Methods Appl. Mech. Eng. 193 (2004) 4097–4116.

[47] N.M. Newmark, A method of computation for structured dynamics, ASCE J. Eng. Mech. Div. 85 (1959) 67–94.

[48] Y. Xu, Y.T. Peet, Accuracy and performance of fluid-structure interaction algorithms with explicit versus implicit formulations of the fluid solver, AIAA Paper 2017–3449 in: 23rd AIAA Computational Fluid Dynamics Conference, AIAA Aviation Forum and Exposition, Denver, CO, June 2017, 2017.

[49] S. Patel, P. Fischer, M. Min, A. Tomboulides, A characteristic-based spectral element method for moving domain problems, J. Sci. Comput. 79 (2019) 564–592.

[50] P.D. Thomas, C.K. Lombard, Geometric conservation law and its application to flow computations on moving grids, AIAA J. 17 (1979) 1030–1037.

[51] H. Guillard, C. Farhat, On the significance of the geometric conservation law for flow computations on moving meshes, Comput. Methods Appl. Mech. Eng. 190 (2000) 1467–1482.

[52] P. Geuzaine, C. Grandmont, C. Farhat, Design and analysis of ALE schemes with provable second-order time-accuracy for inviscid and viscous flow simulations, J. Comput. Phys. 191 (2000), 296–227.

[53] B. Koobus, C. Farhat, Second-order time-accurate and geometrically-conservative implicit schemes for flow computations on unstructured dynamic meshes, Comput. Methods Appl. Mech. Eng. 170 (1999) 103–129.

[54] P.F. Fischer, An overlapping Schwarz method for spectral element solution of the incompressible Navier-Stokes equations, J. Comput. Phys. 133 (1997) 84–101.

[55] A. Quarteroni, F. Saleri, A. Veneziani, Factorization methods for numerical approximation of Navier-Stokes equations, Comput. Methods Appl. Mech. Eng. 188 (2000) 505–526.

[56] J.V. Kan, A second-order accurate pressure-correction scheme for viscous incompressible flow, SIAM J. Sci. Stat. Comput. 80 (1986) 870–891.

[57] B.E. Merrill, Y.T. Peet, P.F. Fischer, J.W. Lottes, A spectrally accurate method for overlapping grid solution of incompressible Navier-Stokes equations, J. Comput. Phys. 307 (2016) 60–93.

[58] O. Walsh, Eddy solutions of the Navier-Stokes equations, in: J.G. Heywood, K. Masuda, R. Rautmann, V.A. Solonnikov (Eds.), The Navier-Stokes Equations II — Theory and Numerical Methods, vol. 1530, Springer Berlin Heidelberg, Berlin, Heidelberg, 1992, pp. 306–309.

[59] V. Chabannes, G. Pena, C. Prud'homme, High-order fluid-structure interaction in 2D and 3D application to blood flow in arteries, J. Comput. Appl. Math. 246 (2013) 1–9.

[60] R.M. Kirby, M. Berzins, J.S. Hesthaven (Eds.), Spectral and High Order Methods for Partial Differential Equations: Proceedings of ICOSAHOM Conference, ICOSAHOM 2014, Salt Lake City, UT, USA, June 23–27, 2014, Springer, 2014.

[61] S. Xu, D. Rempfer, J. Lumley, Turbulence over a compliant surface: numerical simulation and analysis, J. Fluid Mech. 478 (2003) 11–34.

[62] Q.-J. Xia, W.-H. Huang, C.-X. Xu, Direct numerical simulation of turbulent boundary layer over compliant wall, J. Fluids Struct. 71 (2017) 126–142.

[63] H.O.G. Benschop, A.J. Greidanus, R. Delfos, J. Westerweel, W.-P. Breugem, Deformation of a linear viscoelastic compliant coating in a turbulent flow, J. Fluid Mech. 859 (2019) 613–658.

[64] R. Mittal, G. Iaccarino, Immersed boundary methods, Annu. Rev. Fluid Mech. 37 (2005) 239–261.

[65] J. Kim, P. Moin, R. Moser, Turbulence statistics in fully developed channel flow at low Reynolds number, J. Fluid Mech. 177 (1987) 133–166.

[66] M.A. Sprague, M. Churchfield, A. Purkayastha, P. Moriarty, S. Lee, A comparison of Nek5000 and OpenFOAM for DNS of turbulent channel flow, https://www.mcs.anl.gov/~fischer/nek5000/sprague_nek5000_dec2010.pdf, 2010.

[67] K.M. Butler, B.F. Farrell, Three-dimensional optimal perturbations in viscous shear flow, Phys. Fluids A, Fluid Dyn. 4 (1992) 1637–1650.

[68] J. Jiménez, On the structure and control of near wall turbulence, Phys. Fluids 6 (1994) 944–953.

[69] J.M. Hamilton, J. Kim, F. Waleffe, Regeneration mechanisms of near-wall turbulence structures, J. Fluid Mech. 287 (1995) 317–348.

[70] M. Luhar, A.S. Sharma, B.J. McKeon, A framework for studying the effect of compliant surfaces on wall turbulence, J. Fluid Mech. 768 (2015) 415–441.

[71] T. Lee, M. Fisher, W.H. Schwarz, Investigation of the effects of a compliant surface on boundary-layer stability, J. Fluid Mech. 288 (1995) 37–58.

[72] R.J. Adrian, Hairpin vortex organization in wall turbulence, Phys. Fluids 19 (2007) 041301.

[73] Y. Peet, P. Sagaut, Y. Charron, Pressure loss reduction in hydrogen pipelines by surface restructuring, Int. J. Hydrog. Energy 34 (2009) 8964–8973.

[74] D.J. Coxe, Drag Reduction in Turbulent Pipe Flow by Transverse Wall Oscillations at Low and Moderate Reynolds Number, Master's Thesis, Arizona State University, 2019.

[75] P. Causin, J. Gerbeau, F. Nobile, Added-mass effect in the design of partitioned algorithms for fluid-structure problems, Comput. Methods Appl. Mech. Eng. 194 (2005) 4506–4527.

[76] C. Förster, W.A. Wall, E. Ramm, Artificial added mass instabilities in sequential staggered coupling of nonlinear structures and incompressible viscous flows, Comput. Methods Appl. Mech. Eng. 196 (2007) 1278–1293.